frontiers | Frontiers in Earth Science

TYPE Original Research
PUBLISHED 29 September 2025
DOI 10.3389/feart.2025.1588243

OPEN ACCESS

EDITED BY
Abderrahmane Bendaoud,
University of Science and Technology Houari Boumediene, Algeria

REVIEWED BY
Yinhang Cheng,
China Geological Survey, China
Mohamed Faisal,
Suez Canal University, Egypt

*CORRESPONDENCE
Wei-Cheng Ding,
17817717@qq.com
Bin Liu,
13951651882@163.com

RECEIVED 05 March 2025
ACCEPTED 29 August 2025
PUBLISHED 29 September 2025

CITATION
Hu P, Ding W-C, Liu B, Wei W-F, Qi J-M and Qiu L (2025) Geochronology and geochemistry of the Fogang granitic batholith and its implications for uranium mineralization.
Front. Earth Sci. 13:1588243.
doi: 10.3389/feart.2025.1588243

Geochronology and geochemistry of the Fogang granitic batholith and its implications for uranium mineralization

Peng Hu[1,2,3], Wei-Cheng Ding[1,2]*, Bin Liu[1,2,3,4]*, Wen-Fang Wei[5], Jia-Ming Qi[3] and Liang Qiu[6]

[1]College of Nuclear Technology and Automation Engineering, Chengdu University of Technology, Chengdu, China, [2]Applied nuclear technology of in Geosciences key laboratory of Sichuan province, Chengdu university of technology, Chengdu, China, [3]Research Institute No. 290, China National Nuclear Corporation, Shaoguan, China, [4]State Key Laboratory for Mineral Deposits Research, School of Earth Sciences and Engineering, Nanjing University, Nanjing, China, [5]Research Institute Shaanxi Yanchang Petroleum (Group) Co., Ltd., Xi'an, China, [6]School of Earth Sciences and Resources, China University of Geosciences, Beijing, China

The E–W-striking Fogang granitic batholith represents the largest composite batholith in Guangdong Province. To date, the only known uranium deposit, the Pajiang deposit, has been identified in the southwestern portion of the Fogang granitic batholith. This deposit is hosted by porphyritic biotite granite (PBG) and two-mica granites. Nevertheless, the age, petrogenesis, and genetic relationships between these lithologies and the associated uranium mineralization remain subjects of ongoing debate. In this study, zircon U–Pb dating, whole-rock geochemistry, and zircon trace-element analyses of porphyritic biotite granite and two-mica granites in the Pajiang area of the Fogang granitic batholith were systematically investigated. The results reveal that the geochronologies of the porphyritic biotite granite, medium-to-fine-grained two-mica granite (M-FG TMG), and fine-grained two-mica granite (FG TMG) are 156.7 ± 0.7 Ma (MSWD = 0.2, n = 11), 155.3 ± 1.6 Ma (MSWD = 0.5, n = 12), and 153.8 ± 1.4 Ma (MSWD = 0.6, n = 24), respectively. The porphyritic biotite granite is characterized by high SiO_2, high alkalis, and a metaluminous to peraluminous composition (A/CNK = 0.95–1.21; mean = 1.08) but low rare earth contents (∑REE: 107 ppm–465 ppm, mean = 183 ppm) and negative Eu anomalies (δEu = 0.12–0.60, mean = 0.29), indicative of a highly fractionated S-type granite. The porphyritic biotite granite, medium-to-fine-grained two-mica granite, and fine-grained two-mica granite all show high Rb/Sr values (1.52–41.7, with a mean of 8.76), indicating derivation from mature continental crust material. The porphyritic biotite granite has CaO/Na_2O ratios of 0.06–0.70, suggesting that its source was a mixture of pelitic and clastic rocks. The medium-to-fine-grained two-mica granite and fine-grained two-mica granite have lower CaO/Na_2O ratios, indicating derivation from predominantly pelitic sources. Zircon trace-element data indicate that the porphyritic biotite granite has a relatively higher oxygen fugacity (fO_2 = –13.2), followed by the medium-to-fine-grained two-mica granite and the fine-grained two-mica granite, which exhibit relatively

lower oxygen fugacities (fO_2 = −20.2 and −17.3, respectively). Under low-oxygen-fugacity conditions, uranium tends to crystallize as independent uranium-bearing minerals or uranium-rich minerals during the magmatic stage; in contrast, under high-oxygen-fugacity conditions, uranium is more likely to be incorporated into refractory accessory minerals (e.g., zircon and monazite). The crystallization processes of the medium-to-fine-grained two-mica granite and the fine-grained two-mica granite are thus particularly favorable for the formation of uranium-bearing minerals such as uraninite and thorite. These minerals are susceptible to dissolution by hydrothermal fluids during subsequent Late Cretaceous uranium mineralization, thereby releasing uranium and providing a substantial source for mineralization. This further suggests that the two-mica granites serve as significant uranium source rocks for granite-type uranium deposits and hold favorable implications for mineral exploration.

KEYWORDS

Fogang granitic batholith, zircon U–Pb dating, S-type granites, whole-rock geochemistry, uranium source, Pajiang area

1 Introduction

In northern Guangdong, there are three nearly east–west-trending granite belts (Figures 1A,B), which, from north to south, are the Zhuguang–Jiufeng granite belt, the Guidong–Dadongshan granite belt, and the Fogang–Xinfengjiang granite belt (Shu et al., 2006). Many granite-hosted uranium deposits, such as those in the Chengkou, Changjiang, Baishun, and Xiazhuang uranium ore fields, have been found in the Zhuguang–Jiufeng and Guidong–-Dadongshan granite belts (Li et al., 2024a). Spatially, these uranium deposits are closely associated with granites, with mineralization distributed both within and along the margins of granitic intrusions.

Granite-hosted uranium deposits in South China predominantly occur within S-type granites, particularly those formed through crustal anatexis during the Triassic and Jurassic periods, with subordinate occurrences in A-type granites. These granitoids are typically enriched in uranium-bearing minerals such as uraninite, which act as the critical metal source for subsequent mineralization events (Tao et al., 2025). Extensive evidence indicates that oxidative meteoric waters effectively leach uranium from uranium-bearing or uranium-rich minerals through fluid–rock interactions, thereby facilitating uranium mobilization and enrichment (Chabiron et al., 2003; Cuney, 2009; Qiu et al., 2015; 2018; Zhang L. et al., 2018; 2021a; Zhang et al., 2019). Economically significant uranium deposits are notably concentrated within large composite batholiths characterized by multiphase and multi-stage emplacement histories (Zhang et al., 2021b; Fan et al., 2023). A critical unresolved issue pertains to identifying which specific phase or emplacement stage within these composite plutons served as the principal uranium source for mineralization or whether the entire composite body contributed uniformly to the uranium endowment. Addressing this question is essential for accurately delineating ore-body distributions and refining exploration strategies. Consequently, systematic investigations aimed at pinpointing the uranium-contributing phase or stage within composite granite plutons represent a key research priority.

The Fogang granitic batholith, a major constituent of the "Fogang–Xinfengjiang Granite Belt," spans an area of approximately 6,000 km^2, making it the largest composite batholith within Guangdong Province (Chen et al., 2002; Xu et al., 2007; Guo and Huang, 2019; Ding et al., 2022). This extensive batholith is primarily composed of porphyritic biotite granite (PBG), medium-to-fine-grained two-mica granite (M-FG TMG), and fine-grained two-mica granite (FG TMG). Previous geological surveys (Guangdong Bureau of Geology and Mineral Resources, Team No.705, 1983; Li et al., 2024b) in the southwestern part of the Fogang granitic batholith have identified the Pajiang uranium deposit, three uranium occurrences (No. 402, 407, and 408; Figure 1B), and multiple anomalous zones, highlighting the considerable potential of the batholith for uranium exploration. However, significant uncertainties remain concerning the formation age, magmatic evolution sequence, and polyphase or multi-stage development of these granitic bodies. Additionally, the specific lithological units responsible for supplying uranium to the identified deposits have yet to be clearly determined. As variations in uranium fertility among different intrusive phases may critically influence the scale of mineralization, it is essential to systematically constrain the temporal evolution of PBG, M-FG TMG, and FG TMG within the Fogang granitic batholith through integrated geochronological and petrochemical investigations. These constraints significantly enhance metallogenic models and exploration targeting efficiency. Controversy also persists regarding the petrogenetic classification of the Fogang granitic batholith. Some scholars, through analyses of trace elements, rare earth elements (REEs), and Sr–Nd–Hf isotopes of the PBG, suggest that it has an I-type affinity (Li et al., 2007; Chen and Yang, 2015). In contrast, other researchers argue for an S-type origin based on analyses of elemental geochemistry and Sr–Nd–Pb–O isotopes (Chen et al., 2002). Therefore, further geochemical and geochronological investigations are essential to resolve this debate and establish a more robust genetic framework for the batholith.

This study, leveraging petrology, zircon U–Pb chronology, geochemistry, and zircon trace element analyses, aims to constrain the formation ages, magmatic evolution, and petrogenetic type of these granitic units. By establishing the link between magmatic processes (e.g., oxygen fugacity variations) and uranium

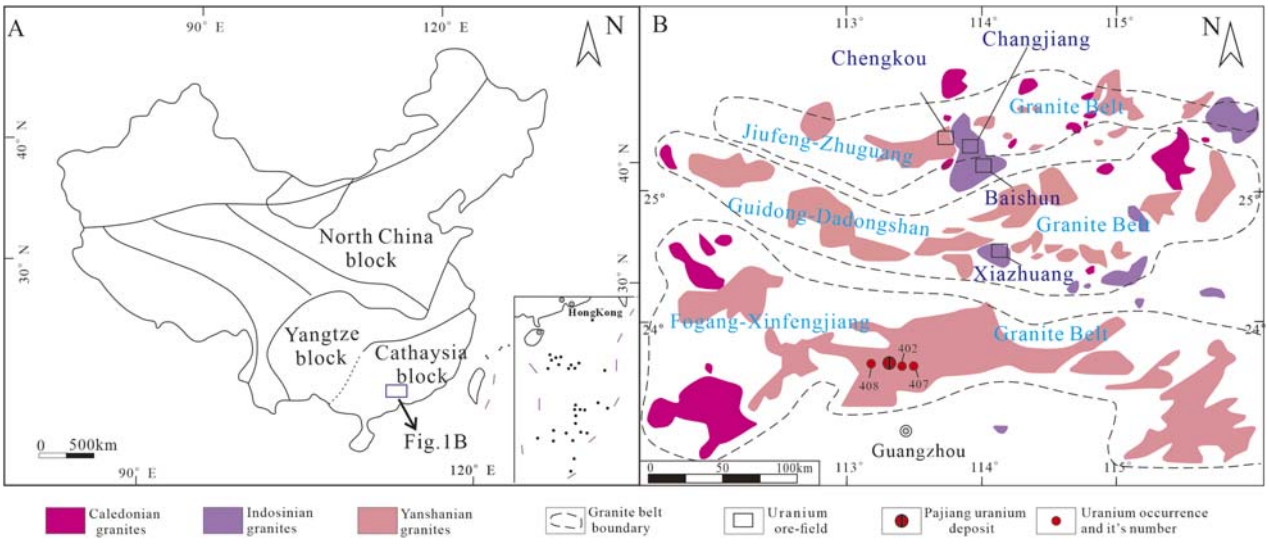

FIGURE 1
(A) Geotectonic position; **(B)** distribution map of east–west-trending granite belts, northern Guangdong (modified after Zhou, 2007).

mineralization potential across different granitic units, this study aims to identify which lithologies (e.g., PBG, M-FG TMG, and FG TMG) serve as primary uranium sources. This, in turn, will refine metallogenic models for granite-type uranium deposits in the region, enabling more targeted and efficient prospecting.

2 Geological setting

The Fogang granitic batholith (23°30′–24°10′N, 113°00′–114°20′E), which is primarily controlled by the Fogang–Fengshun and Enping–Xinfeng faults (Figures 2A,B), extends in an east–west direction along the Fogang–Heyuan region. It spans approximately 140 km in length and 40 km in width. This batholith, a multi-stage composite granitic body (Chen et al., 2002), is primarily composed of PBG, M-FG TMG, and FG TMG in the Pajiang area (Figure 2B). Among these, PBG exhibits the widest exposure, intruding into Devonian and Jurassic strata, while M-FG TMG and FG TMG show relatively smaller exposures.

Since the 1950s, the Pajiang uranium deposit and multiple uranium occurrences have been identified within the Fogang granitic batholith. The Pajiang deposit is situated in the southwestern portion of the Fogang granitic batholith, with its host rocks comprising FG TMG and M-FG TMG. The deposit is structurally controlled by prominent fault systems, notably the nearly east–west-trending Shegang fault and Zhuyuan fault, which exhibit evidence of complex stress regimes, including extensional, compressional, and torsional deformation (Li et al., 2024b; Xu, 2024). These major faults functioned as key ore-guiding structures, facilitating the migration of hydrothermal fluids. In addition to these primary faults, secondary fractures trending sub-NW–SE and nearly N–S are extensively developed within the shear zones. Hydrothermal alteration is pervasive, encompassing silicification, hematitization, sericitization, dark purple fluoritization, pyritization, and chloritization. Among these, silicification—characterized by dark red microcrystalline quartz—along with dark purple fluorite and cloudy hematitization, shows a strong spatial and genetic association with uranium mineralization (Li et al., 2024b). The primary ore minerals include pitchblende and minor coffinite, whereas the gangue minerals are dominated by quartz, pyrite, and dark purple fluorite.

3 Petrography

In this study, fresh granite samples from the Pajiang area were analyzed using petrological and mineralogical methods. The primary rock types identified are PBG, M-FG TMG, and FG TMG.

The PBG is grayish-white with massive structures and is mainly composed of quartz (25–27 wt%), K-feldspar (45–48 wt%), plagioclase (16–20 wt%), and biotite (7–9 wt%, Figure 3A). The quartz is grayish-white and euhedral in shape, mostly over 5 mm in size, and locally encloses zircon and other accessory minerals (Figures 3A,B). K-feldspar is mainly euhedral–subhedral in shape, predominantly microcline, developing lattice double crystals and stripe structures (Figure 3C), and is slightly altered by sericitization. Plagioclase is grayish-white with euhedral–subhedral shapes, exhibiting albite twinning, An = 28, partly altered by sericitization. Biotite is brown, flaky, 2–5 mm in size, and exhibits pale yellow to yellow–brown pleochroism. The accessory minerals include zircon, apatite, and allanite, among which allanite is relatively more enriched (Figure 3C).

The M-FG TMG is grayish-white with a massive structure (Figure 3D). It is mainly composed of quartz (25–28 wt%), K-feldspar (44–48 wt%), plagioclase (15–20 wt%), biotite (5–6 wt%), and muscovite (5–6 wt%). Quartz is grayish-white and euhedral in shape, with a particle size of 1–4 mm, and exhibits undulatory extinction locally (Figure 3E). K-feldspar is predominantly euhedral to subhedral in form, with a grain size of 2–4 mm, and exhibits slight alteration by sericitization (Figure 3E). Plagioclase also appears

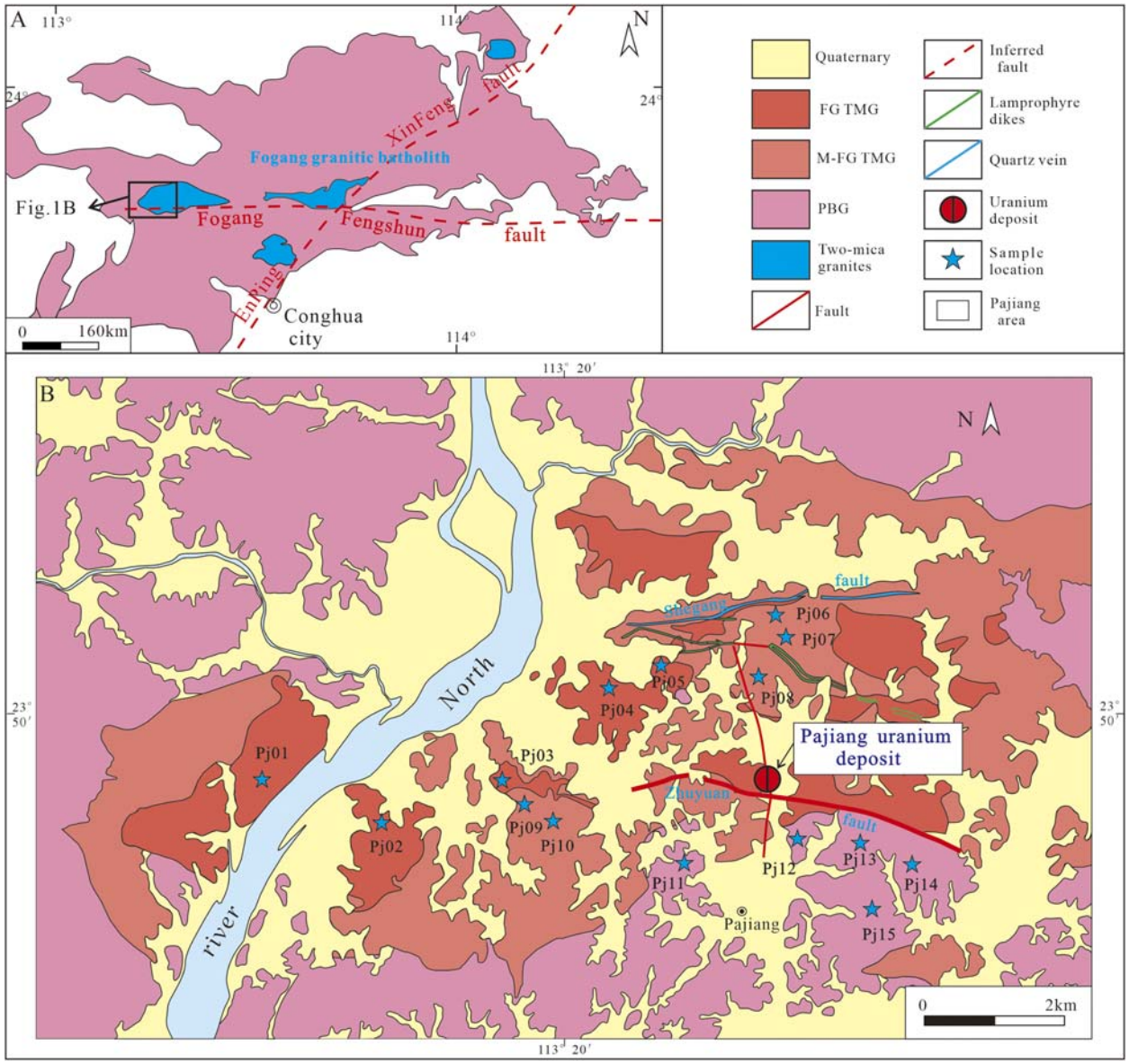

FIGURE 2
(A) Geological sketch map of the Fogang granitic batholith. **(B)** Geological sketch map of the Pajiang area.

mainly as euhedral to subhedral crystals, often occurring in clustered twin forms, and shows alteration by sericitization and muscovitization (Figures 3E,F). Biotite, typically ranging from 1 to 3 mm in size, is partially altered to chlorite and locally encloses certain accessory minerals, such as zircon (Figure 3F). The accessory minerals include zircon and apatite.

The FG TMG, exhibiting a massive structure (Figure 3G), is primarily composed of quartz (25–27 wt%), K-feldspar (45–48 wt%), plagioclase (16–18 wt%), biotite (4–5 wt%), and muscovite (4–5 wt%). Quartz is grayish-white and euhedral in shape, and its particle size is 1–2 mm (Figure 3H); K-feldspar is mainly euhedral–subhedral in shape, developing lattice double crystals, and is slightly altered by sericitization (Figure 3H). Plagioclase is mainly euhedral–subhedral in shape and is altered by sericitization and muscovitization (Figure 3H). Biotite, with a size of 1–2 mm, is partly altered by chlorite and is commonly associated with pyrite (Figure 3I). The accessory minerals, such as zircon and apatite, can be found locally.

4 Sampling and analytical methods

In this study, five FG TMG samples (Pj01–Pj05), five M-FG TMG samples (Pj06–Pj10), and five PBG samples (Pj11–Pj15) were collected from the Pajiang area for zircon separation and geochemical analysis.

Laser ablation inductively coupled plasma mass spectrometer (LA-ICP-MS) analysis, zircon U–Pb dating, and trace element

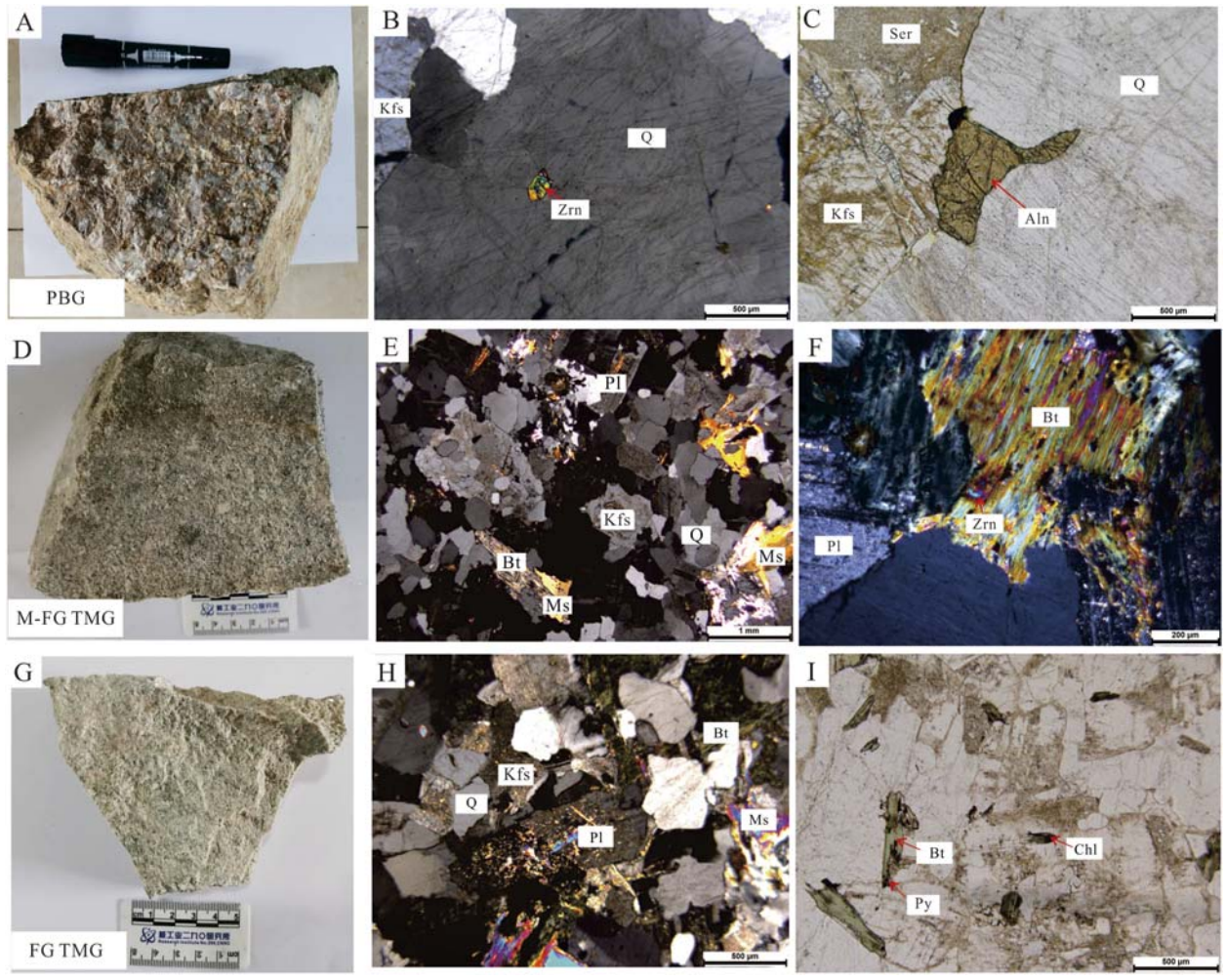

FIGURE 3
Hand specimens and photomicrographs of rocks from the Fogang granitic batholith in the Pajiang area. **(A)** Hand specimens of PBG; **(B)** Coarse-grained quartz enclosing zircon in PBG (Cross-polarized light); **(C)** Sericitization developed in K-feldspar (Plane-polarized light); **(D)** Hand specimens of M-FG TMG; **(E)** Photomicrographs of M-FG TMG (Cross-polarized light); **(F)** Zircon enclosed in biotite (Cross-polarized light); **(G)** Hand specimens of FG TMG; **(H)** Photomicrographs of FG TMG (Cross-polarized light); **(I)** Chloritization of biotite (Plane-polarized light). Q, quartz; Kfs, feldspar; Pl, plagioclase; Bt, biotite; Ms, muscovite; Chl, chlorite; Ser, sericite; Zrn, zircon; Py, pyrite; Aln, allanite.

analysis were carried out on the collected samples from the Pajiang area. Zircon crystals were separated from bulk rock samples using standard magnetic and density separation techniques, followed by manual extraction under a binocular microscope. The selected zircon grains were embedded in an epoxy mount. Prior to analysis, cathodoluminescence (CL) and backscattered electron (BSE) imaging were conducted at the Wuhan Sample Solution Analytical Technology Company to characterize internal textures and identify suitable target sites for U–Pb isotopic analysis. Zircon U–Pb isotope analysis was carried out via LA-ICP-MS at the Wuhan Sample Solution Analytical Technology Company, using an Agilent 7900 instrument. A 32 μm spot size was adopted in this study. Helium was used as the carrier gas to increase the transport efficiency of the ablated material. Data were acquired for 20 s with the laser off and 40 s with the laser on. Glass NIST610 was used as the external calibration standard, while Zircon 91500 served as the internal standard for U–Pb dating and trace element calibration (Hu et al., 2015), respectively. The ages and concordia diagrams were prepared using ISOPLOT 3.0 (Ludwig, 2003).

Major oxide concentrations were determined using a PANalytical (formerly Philips) PW 2424 X-ray Fluorescence (XRF) Spectrometer at American Laboratory Services Chemex (Guangzhou) Company Limited, China, with analytical uncertainties controlled within ≤ 2 wt%. Trace and REE contents were analyzed at the same facility using an Agilent 7900 Quadrupole Inductively Coupled Plasma Mass Spectrometer. Approximately 50 mg of each powdered rock sample was utilized for trace element analysis. All samples underwent digestion in distilled HF and HNO_3 within Teflon screw-cap capsules at 190 °C for 72 h, followed by drying and a secondary digestion in HNO_3 at 150 °C for 24 h. The final step was repeated once. The dissolved samples were diluted to 49 mL with 3 wt% HNO_3 and 1 mL of 500 ppb. Rh was added to the solution as an internal standard. The analytical uncertainties for trace elements and REE were generally lower than 10 wt%.

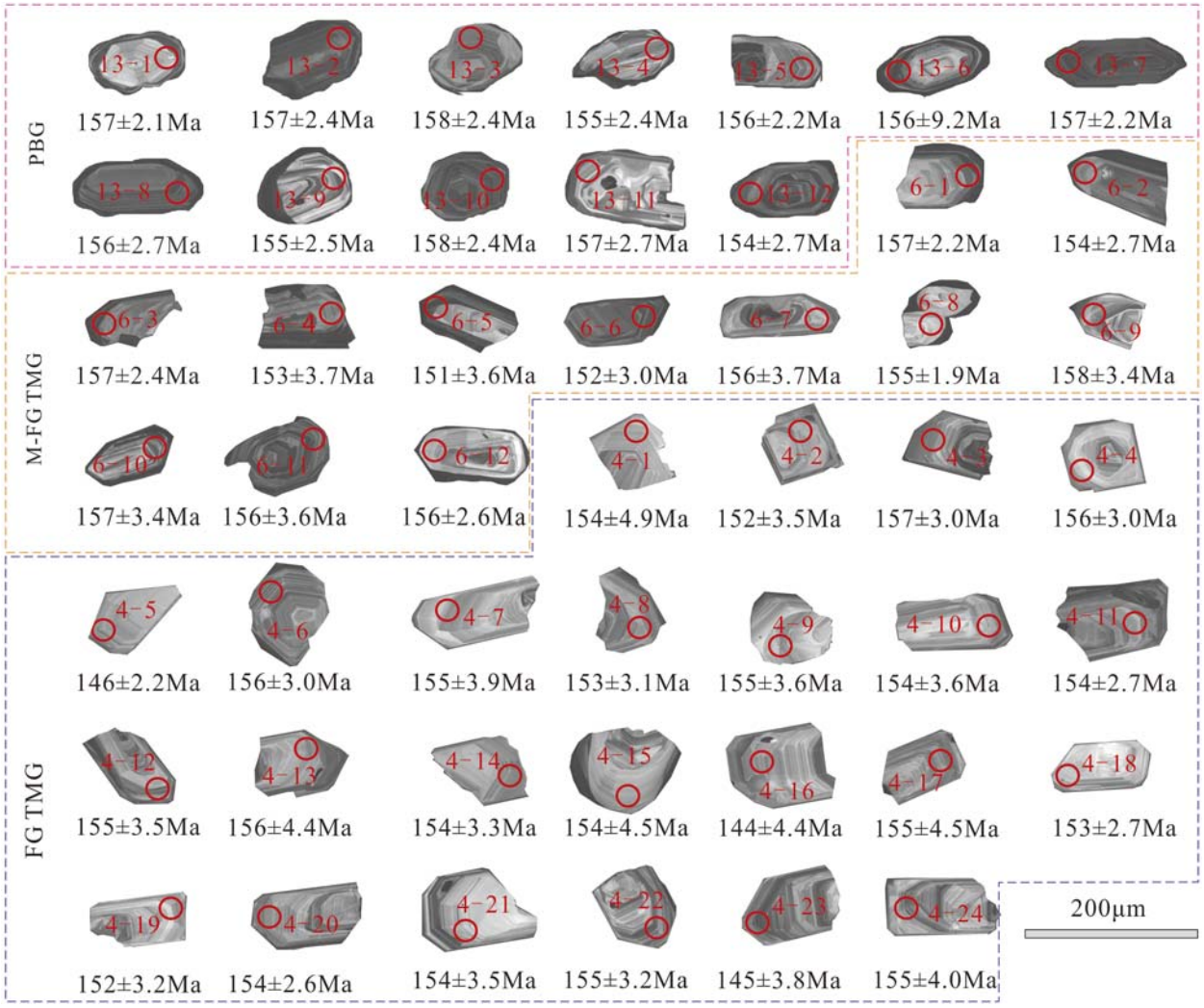

FIGURE 4
Cathode luminescence images of zircon grains from the granites in the Fogang granitic batholith.

5 Results

5.1 U–Pb zircon ages and zircon Ti–temperature calculations

The zircon grains from the three types of granite are mostly euhedral, transparent, and colorless. CL imaging reveals distinct core–rim structures with well-defined oscillatory zoning growth bands (Figure 4). The Th/U ratios of zircon in PBG, M-FG TMG, and FG TMG range from 0.03 to 0.54 (mean = 0.24), 0.13 to 0.55 (mean = 0.31), and 0.43 to 0.72 (mean = 0.54), respectively (Table 1), indicating a magmatic origin (Li et al., 2014; Yang et al., 2024).

A total of 12 spots in the PBG samples were analyzed (Table 1). The results indicate that the $^{206}Pb/^{238}U$ and $^{207}Pb/^{235}U$ ages are mostly concordant, with all spots lying on the concordia line. A data point to the right of the concordia line was excluded as its deviation was likely due to Pb loss. The remaining 11 data points show that the $^{206}Pb/^{238}U$ ages mainly range from 155 to 158 Ma. The analyzed grains yield a weighted mean $^{206}Pb/^{238}U$ age of 156.7 ± 0.7 Ma (MSWD = 0.2, n = 11) (Figures 5A,B), indicating the product of Yanshanian magmatic activity.

A total of 12 spots of M-FG TMG zircons were analyzed, with all data points lying on the concordia line. Furthermore, $^{206}Pb/^{238}U$ ages were concentrated in the range of 151–158 Ma, with a weighted average age of 155.3 ± 1.6 Ma (MSWD = 0.5, n = 12) (Figures 5C,D). A total of 24 spots in the FG TMG samples were analyzed, and the $^{206}Pb/^{238}U$ ages were concentrated in the range of 144–157 Ma, with a weighted mean $^{206}Pb/^{238}U$ age of 153.8 ± 1.4 Ma (MSWD = 0.6, n = 24) (Figures 5E,F). The ages of the M-FG TMG and FG TMG are consistent with those of the PBG, indicating the product of contemporaneous intrusion magmatism.

Additionally, the relationship between zircon Ti content and temperature was utilized, using the formula logTi (ppm) = (5.711 ± 0.072)– (4800 ± 86)/T (K) $-\log\alpha_{SiO2} + \log\alpha_{TiO2}$ (Ferry and Watson, 2007),where T is the temperature in Kelvin, and Ti is the content of titanium in zircon. Owing to the occurrence of quartz and rutile as independent minerals in rocks, with $\alpha_{SiO2} \approx 1$ and $\alpha_{TiO2} \approx 0.6$ (Li et al., 2021; Li et al., 2022), zircon Ti–temperature calculations

TABLE 1 Results of LA-ICP-MS zircon U–Pb dating for the granites in the Fogang granitic batholith.

Lithology and sample No.	Grain spot	ppm		Th/U	Isotopic ratio						Age (Ma)					
		Th	U		$^{207}Pb/^{206}Pb$	1σ	$^{207}Pb/^{235}U$	1σ	$^{206}Pb/^{238}U$	1σ	$^{207}Pb/^{206}Pb$	1σ	$^{207}Pb/^{235}U$	1σ	$^{206}Pb/^{238}U$	1σ
PBG (Pj13)	13-1	193	494	0.39	0.0483	0.0023	0.1634	0.0075	0.0247	0.0003	122	111.1	154	6.6	157	2.1
	13-2	146	1209	0.12	0.0499	0.0016	0.1688	0.0052	0.0246	0.0004	187	75.9	158	4.5	157	2.4
	13-3	187	1628	0.11	0.0511	0.0014	0.1744	0.0050	0.0248	0.0004	243	58.3	163	4.4	158	2.4
	13-4	106	1140	0.09	0.0469	0.0016	0.1569	0.0053	0.0243	0.0004	56	72.2	148	4.7	155	2.4
	13-5	227	433	0.53	0.0518	0.0027	0.1759	0.0100	0.0245	0.0003	276	120.4	165	8.6	156	2.2
	13-6	67	2410	0.03	0.0555	0.0034	0.1786	0.0109	0.0245	0.0015	435	132.4	167	9.4	156	9.2
	13-7	93	1087	0.09	0.0479	0.0015	0.1623	0.0054	0.0246	0.0004	95	74.1	153	4.7	157	2.2
	13-8	203	379	0.54	0.0501	0.0028	0.1688	0.0095	0.0246	0.0004	198	129.6	158	8.2	156	2.7
	13-9	119	2065	0.06	0.0515	0.0044	0.1736	0.0147	0.0244	0.0004	265	196.3	163	12.7	155	2.5
	13-10	302	567	0.53	0.0488	0.0023	0.1671	0.0077	0.0249	0.0004	139	113.9	157	6.7	158	2.4
	13-11	101	631	0.16	0.0495	0.0020	0.1679	0.0069	0.0246	0.0004	172	94.4	158	6.0	157	2.7
	13-12	189	736	0.26	0.0522	0.0020	0.1766	0.0067	0.0246	0.0004	300	82.4	165	5.8	157	2.7
M-FG TMG (Pj06)	06-1	164	623	0.26	0.0475	0.0023	0.1614	0.0071	0.0247	0.0004	72	114.8	152	6.2	157	2.2
	06-2	340	2126	0.16	0.0498	0.0018	0.1661	0.0067	0.0241	0.0004	187	117.6	156	5.8	154	2.7
	06-3	506	926	0.55	0.0482	0.0019	0.1643	0.0067	0.0247	0.0004	109	99.1	154	5.8	157	2.4
	06-4	192	552	0.35	0.0549	0.0034	0.1808	0.0105	0.0240	0.0006	409	138.9	169	9.1	153	3.7
	06-5	194	1541	0.13	0.0466	0.0020	0.1511	0.0061	0.0238	0.0006	28	103.7	143	5.3	151	3.6
	06-6	160	395	0.40	0.0513	0.0027	0.1679	0.0082	0.0239	0.0005	254	122.2	158	7.1	152	3.0
	06-7	180	1245	0.14	0.0485	0.0017	0.1633	0.0054	0.0245	0.0006	124	81.5	154	4.7	156	3.7

(Continued on the following page)

10.3389/feart.2025.1588243

TABLE 1 (*Continued*) Results of LA-ICP-MS zircon U–Pb dating for the granites in the Fogang granitic batholith.

Lithology and sample No.	Grain spot	ppm		Th/U	Isotopic ratio						Age (Ma)					
		Th	U		$^{207}Pb/^{206}Pb$	1σ	$^{207}Pb/^{235}U$	1σ	$^{206}Pb/^{238}U$	1σ	$^{207}Pb/^{206}Pb$	1σ	$^{207}Pb/^{235}U$	1σ	$^{206}Pb/^{238}U$	1σ
	06-8	243	1659	0.15	0.0482	0.0021	0.1611	0.0066	0.0243	0.0003	106	97.2	152	5.8	155	1.9
	06-9	403	1461	0.28	0.0483	0.0016	0.1652	0.0063	0.0248	0.0005	122	75.9	155	5.5	158	3.4
	06-10	346	702	0.49	0.0499	0.0021	0.1690	0.0073	0.0246	0.0005	191	91.7	159	6.4	157	3.4
	06-11	352	871	0.40	0.0471	0.0024	0.1586	0.0079	0.0245	0.0006	54	118.5	150	7.0	156	3.6
	06-12	397	863	0.46	0.0491	0.0033	0.1670	0.0118	0.0246	0.0004	154	148.1	157	10.2	156	2.6
FG TMG (Pj04)	04-1	501	1145	0.44	0.0549	0.0028	0.1813	0.0082	0.0241	0.0008	409	108.3	169	7.1	154	4.9
	04-2	313	726	0.43	0.0518	0.0021	0.1694	0.0070	0.0239	0.0006	276	89.8	159	6.1	152	3.5
	04-3	290	598	0.48	0.0494	0.0023	0.1684	0.0092	0.0246	0.0005	169	111.1	158	8.0	157	3.0
	04-4	465	790	0.59	0.0463	0.0026	0.1552	0.0080	0.0245	0.0005	17	125.9	147	7.0	156	3.0
	04-5	254	524	0.49	0.0541	0.0026	0.1717	0.0082	0.0230	0.0003	376	107.4	161	7.1	146	2.2
	04-6	269	460	0.59	0.0468	0.0027	0.1581	0.0095	0.0245	0.0005	39	133.3	149	8.3	156	3.0
	04-7	147	260	0.57	0.0467	0.0054	0.1549	0.0176	0.0244	0.0006	35	251.8	146	15.5	155	3.9
	04-8	231	392	0.59	0.0500	0.0033	0.1636	0.0099	0.0240	0.0005	195	151.8	154	8.7	153	3.1
	04-9	226	423	0.53	0.0479	0.0035	0.1617	0.0124	0.0243	0.0006	98	162.9	152	10.8	155	3.6
	04-10	253	438	0.58	0.0513	0.0025	0.1689	0.0076	0.0242	0.0006	254	113.9	158	6.6	154	3.6
	04-11	221	395	0.56	0.0544	0.0033	0.1810	0.0106	0.0242	0.0004	387	132.4	169	9.1	154	2.7
	04-12	264	505	0.52	0.0474	0.0029	0.1570	0.0093	0.0243	0.0006	78	131.5	148	8.2	155	3.5
	04-13	129	215	0.60	0.0468	0.0041	0.1570	0.0135	0.0246	0.0007	35	200.0	148	11.9	156	4.4
	04-14	165	281	0.59	0.0534	0.0037	0.1782	0.0128	0.0242	0.0005	346	155.5	166	11.0	154	3.3
	04-15	162	296	0.55	0.0547	0.0063	0.1762	0.0163	0.0242	0.0007	398	258.3	165	14.1	154	4.5

(Continued on the following page)

10.3389/feart.2025.1588243

TABLE 1 (*Continued*) Results of LA-ICP-MS zircon U–Pb dating for the granites in the Fogang granitic batholith.

Lithology and sample No.	Grain spot	ppm		Th/U	Isotopic ratio						Age (Ma)					
		Th	U		$^{207}Pb/^{206}Pb$	1σ	$^{207}Pb/^{235}U$	1σ	$^{206}Pb/^{238}U$	1σ	$^{207}Pb/^{206}Pb$	1σ	$^{207}Pb/^{235}U$	1σ	$^{206}Pb/^{238}U$	1σ
	04-16	196	357	0.55	0.0509	0.0054	0.1564	0.0160	0.0226	0.0007	239	238.9	148	14.1	144	4.4
	04-17	153	302	0.51	0.0512	0.0041	0.1709	0.0133	0.0243	0.0006	256	183.3	160	11.6	155	3.5
	04-18	334	461	0.72	0.0497	0.0025	0.1644	0.0078	0.0241	0.0004	183	114.8	155	6.8	153	2.7
	04-19	124	224	0.55	0.0490	0.0040	0.1589	0.0117	0.0239	0.0005	150	177.8	150	10.3	152	3.2
	04-20	275	554	0.50	0.0531	0.0029	0.1777	0.0098	0.0242	0.0004	345	124.1	166	8.5	154	2.6
	04-21	122	256	0.48	0.0509	0.0032	0.1691	0.0106	0.0242	0.0006	239	144.4	159	9.2	154	3.5
	04-22	180	344	0.52	0.0489	0.0028	0.1642	0.0090	0.0244	0.0005	139	−33.3	154	7.8	155	3.2
	04-23	135	275	0.49	0.0586	0.0063	0.1823	0.0192	0.0228	0.0006	550	238.9	170	16.4	145	3.8
	04-24	138	260	0.53	0.0503	0.0041	0.1688	0.0151	0.0243	0.0006	209	190.7	158	13.1	155	4.0

10.3389/feart.2025.1588243

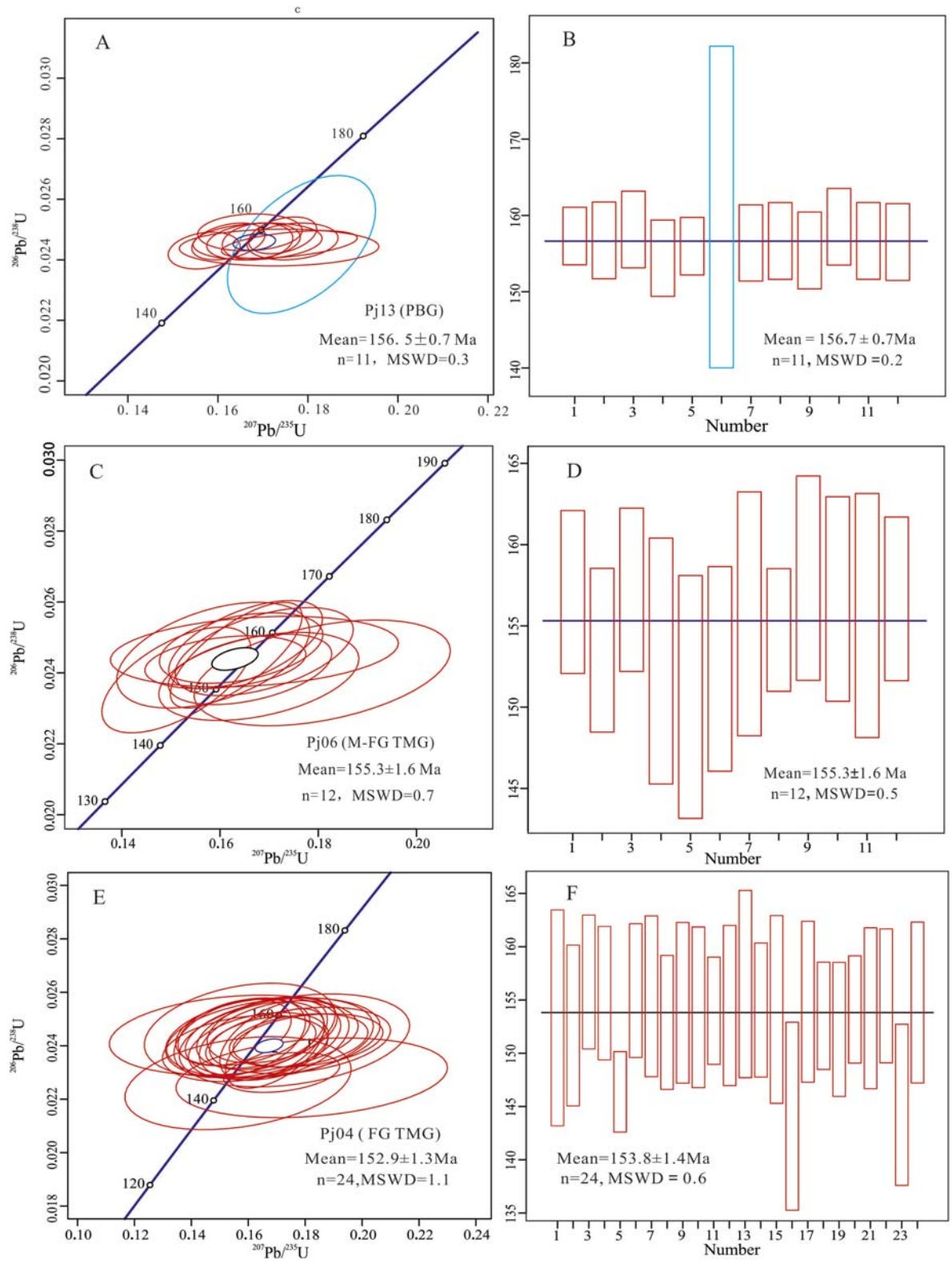

FIGURE 5
U–Pb concordia diagrams of zircons from the granites in the Fogang granitic batholith. **(A)** Concordant age of PBG; **(B)** $^{206}Pb/^{238}U$ average age of PBG; **(C)** Concordant age of M-FG TMG; **(D)** $^{206}Pb/^{238}U$ average age of M-FG TMG; **(E)** Concordant age of FG TMG; **(F)** $^{206}Pb/^{238}U$ average age of FG TMG.

indicate that the PBG has a crystallization temperature range of 622 °C–775 °C, with an average of 714 °C (Table 2). The M-FG TMG and FG TMG exhibit crystallization temperature ranges of 594 °C–821 °C and 712 °C–842 °C, with average temperatures of 709 °C and 755 °C, respectively.

5.2 Whole-rock geochemistry

5.2.1 Major oxides

The results for the major oxides in PBG, M-FG TMG, and FG TMG are listed in Table 3. The compositions of the major oxides in these rocks are similar, with enrichments in SiO_2, total alkali (K_2O+ Na_2O), and peraluminous characteristics but depletions in CaO, MgO, TiO_2, and P_2O_5. The SiO_2 contents range from 73.2 to 75.9 wt% (mean = 74.4 wt%). The Al_2O_3 contents range from 12.7 to 14.3 wt% (mean = 13.7 wt%). The K_2O contents range from 4.60 to 5.52 wt% (mean = 5.21 wt%). The Na_2O contents range from 2.65 to 3.32 wt% (mean = 3.01 wt%). The K_2O/Na_2O ratios range from 1.52 to 1.96 (mean = 1.73).

In the TAS classification diagram (Figure 6A), all sample data in the Fogang granitic batholith fall in the field of granite. In the SiO_2 vs. K_2O diagram (Figure 6B), all sample data belong to the region of the high-K calc-alkaline and shoshonite series. In the A/CNK vs. A/NK diagram (Figure 6C), most of the sample data are distributed in the metaluminous and peraluminous granite fields, indicating that they are metaluminous to peraluminous granites.

5.2.2 Trace element and rare earth element contents of granites

The trace element and REE contents of the PBG, M-FG TMG, and FG TMG are listed in Table 3. Their primitive mantle-normalized spider diagrams (Figure 7A) are similar, showing enrichment in Rb, Th, and U and depletion of Ba, Nb, Sr, and Ti, which are consistent with those of S-type granites (Lan et al., 2020; Xu et al., 2022). The Nb/Ta ratios of the three types of granites range from 5.25 to 7.56, below the continental crustal value (Nb/Ta = 11, Green, 1995). In the Nb vs. Nb/Ta diagram (Figure 8), both the PBG and two-mica granites plot in the field of partial melting of crustal materials, indicating that they are products of partial melting of crust-derived materials (Ballard et al., 2002; Gao et al., 2005).

The ΣREE contents of PBG, M-FG TMG, and FG TMG are lower than those of A-type granite (ΣREE = 336–346 ppm) in South China (Zhu et al., 2008), ranging from 74.8 to 224.3 ppm, with an average value of 126 ppm. The Light Rare Earth Elements/Heavy Rare Earth Elements (LREE/HREE) ratios vary between 3.70 and 13.1, indicating notable differentiation between LREE and HREE. The chondrite-normalized patterns of REE are enriched in LREE (Figure 7B). The LREE/HREE ratios gradually decrease from PBG to M-FG TMG and FG TMG (11.0 → 7.6 → 6.6), indicating a significant increase in the degree of magmatic fraction. The chondrite-normalized REE patterns exhibit pronounced negative Eu anomalies and positive Ce anomalies, with δEu values ranging from 0.21 to 0.43 and δCe values varying from 0.80 to 1.24.

5.3 Characteristics of rare earth elements in zircon

The rare earth element data of zircon are listed in Table 2. The zircon in the PBG, M-FG TMG, and FG TMG has a high total amount of rare earth elements (ΣREE = 10,910–15,313 ppm). The LREE/HREE ratios vary from 0.00026 to 0.00967, indicating HREE enrichment. The chondrite-normalized REE patterns of zircons from the PBG, M-FG TMG, and FG TMG are very similar (Figure 9).

Zircons from all these rocks have positive Ce anomalies (δCe = Ce/ $\sqrt{La^* Pr}$) and negative Eu anomalies (δEu = Eu/ $\sqrt{Sm^* Gd}$) (Sun and Mcdonough, 1989). The δCe values of zircon in the PBG, M-FG TMG, and FG TMG samples range from 34.6 to 130 (mean = 81.0), 8.56 to 21.5 (mean = 14.6), and 1.28 to 218 (mean = 46.5), respectively. The δEu values of zircon in the three types of granites range from 0.02 to 0.12 (mean = 0.09), 0.03 to 0.26 (mean = 0.13), and 0.02 to 0.16 (mean = 0.09), respectively. In general, compared with M-FG TMG and FG TMG granites, PBG exhibits higher Ce anomalies. However, their Eu anomaly values are essentially similar.

5.4 Zircon (Ce^{4+}/Ce^{3+}) oxygen fugacity barometer

Ce in zircons generally exists in the form of Ce^{4+} and Ce^{3+}. In magmas with relatively high oxygen fugacity, Ce mainly exists in the form of Ce^{4+}; because Ce^{4+} and Zr^{4+} have similar ionic radii and the same valency, a large number of Ce^{4+} ions easily enter zircons, resulting in positive anomalies. Therefore, the redox conditions of magma can be affected by the n (Ce^{4+}/Ce^{3+}) value of zircon.

Zircon data from the lattice-strain model were screened according to the La content (≤ 0.1 ppm) and the lattice-strain model deviation coefficient (δK ≤ 3) (Zou et al., 2019). After removing La-, Pr-, and Eu-sensitive elements, zircon melt partition coefficients $D_{Ce^{3+}}^{zircon/melt}$、$D_{Ce^{4+}}^{zircon/melt}$ are calculated (Xin and Qu, 2008); therefore, we use the Ce^{4+}/Ce^{3+} calculation method proposed by Ballard et al. (2002), in which the Ce^{4+}/Ce^{3+} ratios of zircon are calculated based on a lattice-strain model for mineral-melt partitioning of Ce^{4+} and Ce^{3+} cations (Table 2). The ratios of Ce^{4+}/Ce^{3+} in the PBG, M-FG TMG, and FG TMG in this study range from 10.7 to 149 (average 60.6), 10.7 to 52.4 (average 32.3), and 0.45 to 1.67 (average 0.96), respectively.

Additionally, Trail et al. (2011) and Trail et al. (2012) proposed a novel calibration method for determining the oxygen fugacity of magmatic melts based on Ce concentrations in zircon combined with Ti-in-zircon thermometry. This approach is expressed through the following empirical formula:

$$\ln(Ce/Ce^*)_D = (0.1156 \pm 0.0050) \times \ln(fO_2) + \frac{(13860 \pm 708)}{T} - (6.125 \pm 0.484),$$

$$(Ce/Ce^*)_D = \left(Ce_{Zircon}/(La_{Zircon} \times Pr_{Zircon})^{1/2}/\left(Ce_{chondrite}/(La_{chondrite} \times Pr_{chondrite})^{1/2}\right)\right),$$

where fO_2 is the oxygen fugacity. A linear relationship between the Ce anomaly and the reciprocal of temperature can be established under specific mineral oxidation buffer conditions, such as magnetite–hematite (MH), fayalite–magnetite–quartz (FMQ), and iron–wustite (IW) buffers. In the 1/T versus δCe anomaly

TABLE 2 Trace elements (ppm) and characteristic values of trace elements in zircon after screening.

Lithology	Sample	Analytical spot	La	Ce	Pr	Nd	Sm	Eu	Gd	Tb	Dy	Ho	Er	Tm	Yb	Lu	Hf	U	Th	Y	Pb	Ti	Y/Ho	Ce^{4+}/Ce^{3+}	T/°C	$lgfO_2$	δEu	δCe
PGB	PJ13	1	0.02	5.84	0.03	1.59	3.23	0.17	16.7	6.38	80.9	31.8	131	30.7	324	48.3	12,489	494	193	864	78.8	4.04	27.2	56.6	710	−14.5	0.07	61.9
		2	0.01	5.55	0.03	0.87	3.43	0.18	22.8	9.94	115	39.9	172	38.8	384	56.8	11,896	1209	146	1104	176	2.82	27.7	53.8	680	−15.8	0.06	67.3
		3	0.03	2.77	0.01	0.71	2.55	0.21	18.2	8.86	111	37.2	160	38.7	400	52.8	13,362	1628	187	1126	232	4.54	30.3	26.3	720	−16.1	0.09	34.6
		4	0.01	1.76	0.01	0.86	3.15	0.29	25.0	11.4	124	39.6	161	38.2	387	53.8	13,339	1140	106	1212	161	5.79	30.6	16.4	743	−13.7	0.10	48.7
		5	0.01	15.2	0.07	1.24	3.10	0.17	18.6	6.48	78.6	29.0	129	28.6	287	40.2	11,148	433	227	816	65.3	5.98	28.1	149	746	−10.2	0.07	118
		6	--	1.28	0.02	0.58	1.84	0.20	22.2	12.3	164	56.2	237	57.3	606	75.1	14,078	2410	67	1699	360	6.60	30.2	11.7	755	/	0.09	/
		7	0.02	1.53	0.00	1.29	4.33	0.48	45.5	19.9	209	62.0	243	53.9	520	73.8	10,976	1087	93	1885	155	8.09	30.4	14.1	775	/	0.10	/
		8	0.02	14.7	0.08	1.23	3.96	0.29	17.8	6.57	82.5	30.5	134	29.6	308	43.3	10,436	379	203	848	60.7	7.01	27.8	144	761	−9.8	0.11	107
		9	--	1.18	0.09	1.02	3.67	0.10	45.4	20.1	247	84.3	341	74.3	774	116	12,070	2065	119	2639	281	2.70	31.3	10.7	676	/	0.02	/
		10	0.04	14.4	0.00	0.65	3.49	0.19	20.3	7.79	91.6	35.2	154	34.4	345	44.8	11,134	567	302	943	87.3	3.06	26.8	141	686	/	0.07	/
		11	--	2.04	0.10	1.81	7.85	0.65	42.8	19.1	199	58.3	208	41.6	409	53.4	12,423	631	101	1713	92.1	1.34	29.4	19.1	622	/	0.11	/
		12	0.01	8.75	0.03	1.43	3.15	0.32	20.3	8.25	102	36.8	164	38.8	395	55.8	11,837	736	189	1042	104	3.44	28.3	85.4	696	−12.4	0.12	130
	Average		0.02	6.24	0.04	1.11	3.64	0.27	26.3	11.4	134	45.1	186	42.1	428	59.5	12,099	1065	161	1324	155	4.62	29.0	60.6	714	−13.2	0.09	81.0
M-FG TMG	PJ06	1	--	11.0	0.03	0.22	1.19	0.27	13.3	5.84	84.8	32.3	144	37.7	404	59.4	12,338	623	164	977	90.7	1.66	30.2	45.2	638	/	0.21	/
		2	0.05	5.12	0.11	0.74	2.24	0.47	19.6	8.23	106	35.4	157	37.6	420	67.0	12,033	2126	340	1077	301	0.90	30.4	20.5	594	−26.3	0.22	17.5
		3	1.15	27.1	0.53	4.65	5.46	1.01	25.6	11.0	135	48.6	203	50.3	545	73.8	11,690	926	506	1393	141	3.79	28.6	/	704	−22.2	0.26	8.56
		4	0.10	9.19	0.13	0.69	2.76	0.08	14.5	4.94	74.5	26.9	110	27.1	284	38.1	12,546	552	192	772	80.6	4.25	28.7	37.7	715	−18.4	0.04	20.2
		5	0.08	3.96	0.14	2.43	9.97	1.03	83.7	33.7	353	103	362	75.5	688	91.7	13,256	1541	194	3048	204	6.69	29.7	15.7	756	−19.2	0.11	9.22
		6	0.50	12.7	0.22	3.02	2.74	0.20	15.8	6.10	76.7	27.2	116	26.5	261	37.1	12,171	395	160	759	61.8	4.73	27.9	52.3	724	−20.8	0.09	9.36
		7	--	5.86	0.02	0.91	3.34	0.32	23.8	10.2	132	48.1	212	54.1	562	83.5	12,890	1245	180	1386	181	--	28.8	23.6	/	/	0.11	/

(Continued on the following page)

10.3389/feart.2025.1588243

TABLE 2 (*Continued*) Trace elements (ppm) and characteristic values of trace elements in zircon after screening.

Lithology	Sample	Analytical spot	La	Ce	Pr	Nd	Sm	Eu	Gd	Tb	Dy	Ho	Er	Tm	Yb	Lu	Hf	U	Th	Y	Pb	Ti	Y/Ho	Ce^{4+}/Ce^{3+}	T/°C	$lgfO_2$	δEu	δCe
		8	--	2.78	0.04	1.01	7.09	0.32	46.6	20.6	234	80.2	318	74.3	706	101	12,353	1659	243	2387	244	6.36	29.7	10.7	751	/	0.05	/
		9	0.30	9.94	0.16	0.87	3.09	0.19	21.6	8.84	108	40.3	176	40.4	413	58.3	12,586	1461	403	1138	218	1.49	28.3	/	630	−25.6	0.07	11.1
		10	0.19	14.6	0.17	1.52	4.17	0.10	25.4	8.30	109	38.8	169	39.4	388	52.9	11,404	702	346	1072	111	6.90	27.6	/	759	−16.2	0.03	19.7
		11	0.20	17.4	0.20	2.68	4.88	0.76	31.7	10.1	116	42.1	178	45.7	450	62.8	11,930	871	352	1177	134	12.6	28.0	/	821	−13.1	0.19	21.5
		12	0.02	12.7	--	1.61	2.62	0.14	19.7	7.97	100	40.1	170	41.3	408	54.8	12,810	863	397	1063	132	3.69	26.5	52.4	702	/		/
	Average		0.22	11.0	0.15	1.70	4.13	0.41	28.4	11.3	136	46.9	193	45.8	461	65.1	12,334	1080	290	1354	158	4.43	28.7	32.3	709	−20.2	0.13	14.6
FG TMG	PJ04	1	0.14	11.5	0.13	1.38	4.12	0.25	21.6	8.66	114	43.7	188	47.1	475	59.8	12,227	1145	501	1174	170	4.67	26.9	/	723	−17.8	0.08	21.2
		2	0.04	11.4	0.05	0.70	2.94	0.11	15.9	6.09	79.9	30.7	139	35.1	366	50.7	11,926	726	313	886	103	4.11	28.8	0.51	712	−14.5	0.05	59.4
		3	0.68	14.4	0.26	2.02	2.83	0.24	19.9	7.52	86.4	34.6	156	36.1	364	51.2	11,125	598	290	967	88.2	--	27.9	/	/	−28.6	0.10	8.34
		4	1.11	19.1	0.39	3.35	4.67	0.32	26.5	9.37	117	44.9	194	46.8	474	63.7	11,363	790	465	1243	118	8.53	27.7	/	780	−19.1	0.09	7.13
		5	0.01	14.1	0.02	1.20	3.74	0.29	18.5	6.70	90.0	33.4	148	35.6	370	47.6	11,758	524	254	938	78.0	6.12	28.1	0.87	748	−7.8	0.11	218
		6	0.04	19.8	0.06	1.38	3.57	0.14	19.9	8.59	92.1	34.2	153	35.1	346	45.8	11,621	460	269	956	69.4	7.16	28.0	1.67	763	−9.8	0.05	104
		7	5.97	21.9	1.44	9.99	4.13	0.28	18.1	6.67	78.3	28.7	126	28.8	286	43.5	11,501	260	147	823	41.8	15.3	28.7	/	842	−21.4	0.10	1.83
		8	--	16.9	0.05	1.22	3.47	0.19	20.4	8.31	87.4	32.6	140	32.4	340	46.2	11,644	392	231	907	58.3	5.31	27.8	1.26	735	/	0.07	/
		9	--	13.1	0.02	1.56	3.77	0.23	15.9	5.93	68.7	28.4	128	29.2	291	40.1	11,458	423	226	812	66.9	4.77	28.6	0.74	725	/	0.09	/
		10	5.59	29.4	1.55	10.9	6.46	0.35	22.7	7.88	91.2	35.0	147	33.9	359	46.3	10,998	438	253	939	65.1	4.68	26.8	/	723	−25.9	0.09	2.45
		11	0.02	18.2	0.09	0.89	3.27	0.05	17.3	6.57	78.0	29.5	130	27.5	295	39.7	10,913	395	221	825	59.9	6.16	28.0	1.44	748	−10.4	0.02	107
		12	--	6.15	0.08	0.99	3.86	0.11	22.4	8.94	117	42.9	185	41.5	423	56.5	12,136	505	264	1182	75.4	6.07	27.5	/	747	/	0.03	/
		13	1.29	14.1	0.41	2.66	2.80	0.34	19.3	5.55	79.6	27.7	129	28.7	296	40.7	10,740	215	129	794	32.5	5.28	28.7	/	734	−22.8	0.14	4.76
		14	18.7	51.3	5.14	28.5	8.79	0.74	23.8	7.04	82.5	28.9	128	28.7	304	41.2	11,068	281	165	844	42.8	8.20	29.2	/	776	−25.7	0.16	1.28

(Continued on the following page)

10.3389/feart.2025.1588243

TABLE 2 (*Continued*) Trace elements (ppm) and characteristic values of trace elements in zircon after screening.

Lithology	Sample	Analytical spot	La	Ce	Pr	Nd	Sm	Eu	Gd	Tb	Dy	Ho	Er	Tm	Yb	Lu	Hf	U	Th	Y	Pb	Ti	Y/Ho	Ce^{4+}/Ce^{3+}	T/°C	lgfO_2	δEu	δCe
		15	0.24	12.2	0.25	1.90	2.00	0.23	16.5	6.54	82.3	30.9	124	29.2	287	44.4	10,543	296	162	828	52.8	7.82	26.8	/	771	−17.4	0.12	12.3
		16	0.99	16.8	0.27	1.55	2.62	0.12	22.2	6.79	83.3	30.8	134	29.9	317	41.8	11,389	357	196	856	53.3	14.4	27.8	/	836	−16.2	0.05	7.91
		17	0.53	13.9	0.06	1.55	3.06	0.22	16.1	5.65	67.3	25.1	105	24.7	261	35.8	10,640	302	153	697	44.7	6.43	27.8	/	752	−16.7	0.10	19.3
		18	--	19.8	0.10	1.68	3.83	0.35	25.3	9.95	125	44.0	187	43.0	409	57.9	10,387	461	334	1220	77.6	5.73	27.7	1.66	742	/	0.11	/
		19	--	11.0	0.02	0.56	2.21	0.28	13.7	4.80	62.1	23.8	98.4	23.6	241	34.5	10,661	224	124	671	33.6	4.78	28.3	0.45	725	/	0.16	/
		20	--	13.7	0.01	0.97	2.52	0.10	17.3	7.14	85.9	31.7	130	32.1	310	44.2	11,138	554	275	902	84.0	7.90	28.5	0.82	772	/	0.05	/
		21	0.11	9.44	0.13	0.77	1.75	0.14	12.6	5.38	68.1	24.2	113	26.8	274	36.1	10,837	256	122	719	41.1	6.53	29.7	/	754	−16.6	0.09	19.2
		22	0.49	15.0	0.23	2.01	2.59	0.19	15.7	5.80	73.9	26.6	115	26.3	267	36.8	10,646	344	180	751	51.8	8.48	28.2	/	779	−17.5	0.09	10.9
		23	0.05	12.0	0.06	1.11	3.30	0.29	18.3	6.36	83.8	30.1	123	32.2	316	42.1	10,770	275	135	845	41.8	5.35	28.1	0.59	735	−13.8	0.11	52.3
		24	0.02	11.8	0.01	0.00	3.14	0.20	12.4	5.20	66.3	24.5	106	25.0	244	35.1	10,376	260	138	682	40.1	5.93	27.8	0.57	745	−8.6	0.10	180
	Average		1.50	16.5	0.45	3.29	3.56	0.24	18.8	6.98	85.8	32.0	138	32.5	330	45.1	11,161	437	231	894	66.3	6.66	28.1	0.96	755	−17.3	0.09	46.5

"--"indicates data under the detection limit; the samples in this paper are screened according to the chemical standard of "clean zircon" (Zou et al., 2019), and only the trace data from zircon with La ≤ 0.1 ppm are considered in the calculation of Ce^{4+}/Ce^{3+} value; "/" indicates missing data for this item.

$(Ce^{4+}/Ce^{3+})_{zircon} = \left(Ce_{melt} - Ce_{zircon}/D_{Ce^{3+}}^{zircon/melt}\right)/\left(Ce_{zircon}/D_{Ce^{4+}}^{zircon/melt} - Ce_{melt}\right)$, where Ce_{melt} is equivalent to the whole-rock (as a proxy for melt) concentration of Ce, Ce_{zircon} is the concentration of Ce in zircon, $D_{Ce^{3+}}^{zircon/melt}$ and $D_{Ce^{4+}}^{zircon/melt}$ are the partition coefficients for Ce^{3+} and Ce^{4+}, respectively, which can be estimated based on crystal chemical constraints on trace-element partitioning.

Log (ppm Ti-in-zircon) = (5.711 ± 0.072) − (4800 ± 86)/T(K) − logαSiO_2 + logαTiO_2.

$\ln(Ce/Ce^*)_D = (0.1156 \pm 0.0050) \times \ln fO_2 + (13{,}860 \pm 708)/T(K) - (6.125 \pm 0.48)$, where fO_2 is the oxygen fugacity and T is the temperature in Kelvin.

10.3389/feart.2025.1588243

10.3389/feart.2025.1588243

TABLE 3 Major oxides (wt%) and trace element (ppm) compositions of representative samples from the Fogang granitic batholith[§].

No.	PJ01	PJ02	PJ03	PJ04	PJ05	PJ06	PJ07	PJ08	PJ09	PJ10	PJ11	PJ12	PJ13	PJ14	PJ15
	FG TMG					M-FG TMG					PBG				
SiO_2	75.2	74.8	74.2	75.8	74.8	74.0	74.3	75.2	73.6	75.9	73.7	73.6	73.8	73.7	73.2
TiO_2	0.12	0.11	0.13	0.07	0.12	0.09	0.08	0.09	0.14	0.09	0.15	0.14	0.14	0.14	0.14
Al_2O_3	13.0	12.7	13.7	13.3	13.9	13.6	14.3	13.6	14.0	13.5	14.2	14.1	14.0	14.0	14.0
$Fe_2O_3^T$	1.55	1.70	1.38	1.20	1.48	1.48	1.29	1.37	1.43	1.14	1.57	1.60	1.56	1.58	1.56
MnO	0.04	0.04	0.04	0.03	0.04	0.04	0.04	0.02	0.03	0.02	0.03	0.03	0.03	0.04	0.04
MgO	0.16	0.13	0.21	0.11	0.26	0.14	0.18	0.12	0.23	0.14	0.25	0.23	0.25	0.25	0.24
CaO	0.76	0.82	0.41	0.28	0.33	0.42	0.31	0.19	0.41	0.17	0.58	0.41	0.55	0.64	0.71
Na_2O	3.04	2.81	3.17	3.30	2.77	3.26	3.32	2.72	3.01	2.65	3.07	3.03	3.02	3.03	3.02
K_2O	5.02	5.52	5.22	5.02	5.33	5.01	5.17	5.02	5.37	4.60	5.41	5.42	5.31	5.37	5.35
P_2O_5	0.06	0.03	0.11	0.05	0.11	0.15	0.12	0.07	0.20	0.06	0.19	0.20	0.19	0.20	0.19
LOI	1.11	1.16	0.85	0.67	0.97	0.78	0.73	1.25	0.84	1.10	1.05	0.96	1.00	1.01	0.99
Total	100.0	99.8	99.4	99.9	100.1	99.0	99.8	99.6	99.3	99.4	100	99.6	99.9	99.9	99.5
Ga	20.4	19.2	22.7	20.7	23.1	22.5	20.7	21.9	24.1	22.7	24.0	23.8	23.7	23.4	23.9
Rb	379	383	420	397	420	397	354	414	393	391	400	393	388	385	393
Sr	45.8	45.7	43.5	26.3	38.1	31.9	51.8	32.1	46.6	25.2	48.5	43.9	44.9	49.0	52.0
Y	31.8	58.2	21.5	34.1	24.0	24.8	20.7	21.5	13.1	20.4	12.9	13.4	14.2	15.6	13.6
Zr	123	126	95.0	56.0	90.0	89.0	69.0	64.0	111	70.0	109	109	111	111	111
Nb	17.8	15.5	18.8	19.3	18.2	20.4	15.7	19.2	19.7	18.6	19.6	19.6	19.6	19.8	19.8
Ba	235	233	269	128	251	151	279	254	417	145	274	263	261	267	272
La	28.4	47.6	24.1	15.6	28.7	22.1	17.9	17.4	27.6	12.5	27.2	24.4	27.1	27.1	25.8
Ce	56.3	76.2	50.8	34.0	58.8	46.2	35.5	34.9	69.8	27.9	58.5	52.4	58.8	57.9	55.3
Pr	6.90	11.5	5.76	3.76	6.62	5.33	4.10	4.32	6.87	3.64	6.78	6.19	6.93	6.89	6.62
Nd	25.9	44.8	21.5	14.2	25.0	20.1	15.4	17.4	25.2	14.4	24.9	22.5	25.2	25.2	24.0
Sm	5.46	9.68	4.53	3.70	5.27	4.66	3.45	4.29	5.81	3.84	5.74	5.30	5.86	5.80	5.61
Eu	0.44	0.65	0.47	0.30	0.46	0.33	0.47	0.41	0.47	0.39	0.48	0.46	0.49	0.50	0.48
Gd	4.82	8.92	3.66	3.95	4.11	4.23	3.21	3.97	4.20	3.97	4.36	4.07	4.54	4.49	4.22
Tb	0.84	1.50	0.62	0.81	0.69	0.75	0.59	0.66	0.60	0.64	0.62	0.60	0.66	0.66	0.61
Dy	4.82	8.91	3.42	5.19	3.86	4.22	3.51	3.43	2.90	3.50	2.93	2.92	3.17	3.35	3.02
Ho	0.99	1.80	0.66	1.07	0.75	0.81	0.66	0.61	0.45	0.60	0.45	0.46	0.50	0.53	0.46
Er	3.00	5.49	1.90	3.34	2.18	2.22	1.85	1.60	1.09	1.55	1.08	1.10	1.16	1.26	1.11
Tm	0.48	0.84	0.31	0.55	0.35	0.33	0.28	0.23	0.14	0.22	0.14	0.15	0.16	0.18	0.15

(Continued on the following page)

TABLE 3 (*Continued*) Major oxides (wt%) and trace element (ppm) compositions of representative samples from the Fogang granitic batholith[§].

No.	PJ01	PJ02	PJ03	PJ04	PJ05	PJ06	PJ07	PJ08	PJ09	PJ10	PJ11	PJ12	PJ13	PJ14	PJ15
	FG TMG					M-FG TMG					PBG				
Yb	3.13	5.54	1.98	3.83	2.37	1.97	1.84	1.33	0.86	1.39	0.88	0.90	0.97	1.06	0.94
Lu	0.51	0.86	0.32	0.58	0.36	0.29	0.28	0.21	0.12	0.21	0.13	0.13	0.13	0.15	0.13
Hf	4.20	4.60	3.20	2.50	3.20	3.10	2.50	2.40	3.50	2.40	3.50	3.40	3.60	3.50	3.60
Ta	3.10	2.93	3.17	3.15	3.22	3.32	2.86	3.66	2.79	3.54	2.64	2.74	2.64	2.62	2.65
Th	37.3	53.5	25.6	18.2	24.6	22.6	16.6	16.4	25.3	16.4	25.8	25.5	26.7	25.3	25.8
U	16.3	13.5	17.9	23.3	21.2	8.17	6.92	17.3	15.6	13.5	12.5	13.7	12.0	16.7	14.0
Ti	780	730	770	440	750	590	560	560	840	550	920	850	870	830	900
Pb	73.0	39.3	52.4	65.2	56.7	32.0	37.8	31.3	50.3	29.1	36.2	36.7	36.8	36.5	36.1
A/NK	1.24	1.19	1.25	1.23	1.34	1.25	1.29	1.37	1.30	1.45	1.30	1.29	1.31	1.30	1.30
A/CNK	1.10	1.05	1.17	1.17	1.27	1.17	1.23	1.33	1.22	1.40	1.18	1.21	1.20	1.17	1.16
DI	92.9	93.0	94.0	95.1	93.2	93.9	93.8	93.8	93.4	93.4	92.7	93.3	92.7	92.5	92.3
Nb/Ta	5.74	5.29	5.93	6.13	5.65	6.14	5.49	5.25	7.06	5.25	7.42	7.15	7.42	7.56	7.47
Zr/Hf	29.3	27.4	29.7	22.4	28.1	28.7	27.6	26.7	31.7	29.2	31.1	32.1	30.8	31.7	30.8
∑LREE	123	190	107	71.6	125	98.7	76.8	78.7	136	62.7	124	111	124	123	118
∑HREE	18.6	33.9	12.9	19.3	14.7	14.8	12.2	12.0	10.4	12.1	10.6	10.3	11.3	11.7	10.6
∑REE	142	224	120	91	140	114	89	91	146	75	134	122	136	135	128
δEu	0.26	0.21	0.35	0.24	0.30	0.23	0.43	0.30	0.29	0.31	0.29	0.30	0.29	0.30	0.30
δCe	0.99	0.80	1.06	1.09	1.05	1.04	1.02	0.99	1.24	1.01	1.06	1.05	1.05	1.04	1.04
1000*Ga/Al	2.97	2.86	3.14	2.93	3.15	3.14	2.74	3.03	3.25	3.17	3.20	3.20	3.19	3.15	3.22
Zr + Nb + Ce + Y	229	276	186	143	191	180	141	140	214	137	200	194	204	204	200
Rb/Sr	8.28	8.38	9.66	15.10	11.02	12.45	6.83	12.90	8.43	15.52	8.25	8.95	8.64	7.86	7.56
Rb/Nb	21.3	24.7	22.3	20.6	23.1	19.5	22.5	21.6	19.9	21.0	20.4	20.1	19.8	19.4	19.8
CaO/Na_2O	0.25	0.29	0.13	0.08	0.12	0.13	0.09	0.07	0.14	0.06	0.19	0.14	0.18	0.21	0.24
Rb/Ba	1.61	1.64	1.56	3.10	1.67	2.63	1.27	1.63	0.94	2.71	1.46	1.49	1.49	1.44	1.44
$CaO + Al_2O_3$	13.8	13.5	14.1	13.6	14.2	14.0	14.6	13.8	14.4	13.7	14.7	14.5	14.6	14.7	14.7
CaO/Al_2O_3	0.06	0.06	0.03	0.02	0.02	0.03	0.02	0.01	0.03	0.01	0.04	0.03	0.04	0.05	0.05
Y + Nb	49.6	73.7	40.3	53.4	42.2	45.2	36.4	40.7	32.8	39.0	32.5	33.0	33.8	35.4	33.4

No.	15FG 06#	15FG 07#	15FG 08#	2KSC 4a*	2KSC 4b*	2KSC 75*	2KSC 79*	2KF 400*	2KF 402*	2KF 403*	2KF 404*	2KF 405*	FG4[§]	FG8-1[§]	FG15-1[§]
	PBG (data from others)														
SiO_2	71.71	74.3	76.24	73.3	76.94	72.71	71.58	72.66	73.39	75.33	75.15	74.31	73.44	75.62	74.58
TiO_2	0.29	0.18	0.11	0.32	0.12	0.18	0.37	0.13	0.11	0.13	0.1	0.16	0.11	0.11	0.25

(Continued on the following page)

TABLE 3 (*Continued*) Major oxides (wt%) and trace element (ppm) compositions of representative samples from the Fogang granitic batholith[§].

No.	15FG 06#	15FG 07#	15FG 08#	2KSC 4a*	2KSC 4b*	2KSC 75*	2KSC 79*	2KF 400*	2KF 402*	2KF 403*	2KF 404*	2KF 405*	FG4[&]	FG8-1[&]	FG15-1[&]
	PBG (data from others)														
Al_2O_3	13.41	13.12	12.44	13.07	12.03	13.46	13.51	14.54	13.96	13.55	13.63	13.7	13.57	12.40	13.48
$Fe_2O_3^T$	3.01	2.47	1.96	2.52	1.35	2.44	3.46	2.21	1.83	2.03	1.72	2.34	1.02	1.38	1.92
MnO	0.11	0.13	0.1	0.06	0.03	0.05	0.07	0.05	0.04	0.05	0.04	0.06	0.04	0.03	0.07
MgO	0.43	0.21	0.1	0.56	0.18	0.22	0.43	0.16	0.12	0.14	0.12	0.19	0.28	0.16	0.39
CaO	1.04	0.65	0.17	2.19	1.03	0.76	1.5	1.14	1.01	0.95	0.94	1.18	1.56	0.96	1.56
Na_2O	2.94	3.02	2.54	3.15	2.95	3.29	2.68	3.3	3.37	2.94	3.08	3.17	2.95	2.85	2.97
K_2O	5.37	5.41	5.9	4.29	5.21	5.64	5.58	4.94	5.92	5.06	4.91	4.63	4.62	5.54	4.62
P_2O_5	0.09	0.05	0.02	0.09	0.04	0.05	0.09	0.04	0.04	0.05	0.03	0.05	0.21	0.02	0.09
LOI	1.16	0.5	0.39	0.71	0.28	0.95	0.7	0.42	0.42	0.44	0.45	0.44	2.03	0.63	0.53
Total	99.56	100.04	99.97	100.27	100.16	99.74	99.95	99.59	100.21	100.67	100.17	100.24	99.83	99.70	100.46
Ga	19.0	18.7	16.4	16.1	13.8	19.2	20.4	19.6	20.2	19.8	19.1	19.7	22.2	18.6	16.8
Rb	397	453	393	239	294	361	324	403	463	442	403	409	415	366	420
Sr	126	61.7	46.5	157	61.3	49.7	80.8	59.1	64.7	54.8	59.8	59.5	54.8	42.5	116
Y	39.5	43	22.6	27.4	10.6	26.5	24.1	39.1	44.5	29	29.9	42.6	13.0	36.1	23.0
Zr	178	155	117	126	109	183	296	97	114	102	94.2	165	75.5	144	178
Nb	20.8	25.8	13.2	14.5	10.8	21	20.5	37.6	30.4	34.6	19.8	26.2	20.2	15.5	18.2
Ba	410	232	92.4	337	55.7	114	153	156	264	229	195	153	161	204	151
La	58.2	40.1	34.2	40.1	32.7	51.3	102	34.7	29	38	32.7	50.7	23.8	43.6	28.5
Ce	110.5	79.7	58.2	76	56.5	104.4	217	70.4	58.1	78.2	65.2	98.5	36.3	74.0	46.5
Pr	12.1	10.1	8.72	9.39	5.68	13.91	26	8.73	7.23	9.49	7.94	12.4	4.50	10.3	6.38
Nd	41.4	36	30.4	32	16.1	49.4	84.7	30.7	25.8	32.9	28.1	40.9	15.9	40.7	23.2
Sm	8.2	8.45	6.14	5.96	1.88	10.4	14.2	6.79	5.81	6.64	5.96	9.11	3.17	8.71	5.22
Eu	0.98	0.59	0.48	0.89	0.36	0.53	0.79	0.43	0.47	0.42	0.44	0.5	0.39	0.52	0.70
Gd	7.49	8	4.96	5.98	1.77	8.5	9.09	6.28	6.06	5.72	5.33	8.3	3.13	8.28	4.84
Tb	1.06	1.16	0.63	0.79	0.29	1.12	1.12	1.12	1.12	0.97	0.92	1.28	—	—	—
Dy	6.46	7.14	3.79	4.84	1.72	5.36	4.91	6.4	7.14	5.09	5.11	6.61	—	—	—
Ho	1.29	1.51	0.75	1.04	0.35	1.04	0.91	1.34	1.55	1.05	1.05	1.38	—	—	—
Er	3.6	4.11	2.13	2.86	1.08	2.61	2.06	3.99	4.55	2.96	3.01	3.99	—	—	—
Tm	0.54	0.62	0.33	0.43	0.2	0.37	0.28	0.63	0.73	0.44	0.47	0.57	—	—	—
Yb	3.45	4.01	2.17	2.8	1.59	2.35	1.84	4.27	4.98	2.8	3.01	3.74	1.14	4.63	3.33
Lu	0.52	0.61	0.33	0.45	0.3	0.39	0.32	0.68	0.78	0.42	0.45	0.63	0.16	0.67	0.49

(Continued on the following page)

TABLE 3 (*Continued*) Major oxides (wt%) and trace element (ppm) compositions of representative samples from the Fogang granitic batholith[§].

No.	15FG 06#	15FG 07#	15FG 08#	2KSC 4a*	2KSC 4b*	2KSC 75*	2KSC 79*	2KF 400*	2KF 402*	2KF 403*	2KF 404*	2KF 405*	FG4[&]	FG8-1[&]	FG15-1[&]
	PBG (data from others)														
Hf	5.4	5.5	4.1	4.71	4.85	6.81	8.01	3.23	3.67	3.26	3.11	6.01	2.72	6.16	6.04
Ta	3.4	3.1	1.8	2.13	1.57	2.16	1.34	3.4	3.08	3.37	1.95	5.8	4.43	2.16	3.26
Th	54.8	66.4	57.4	36.6	44.3	68.2	39	41.8	36.1	43.4	37.2	51	20.6	51.0	53.6
U	11.7	17.2	9.4	8.1	12.8	22.1	17.4	19.9	14.8	15.2	11.7	17.7	29.5	15.3	12.9
Ti	19.0	18.7	16.4	16.1	13.8	19.2	20.4	19.6	20.2	19.8	19.1	19.7	22.2	18.6	16.8
Pb	397	453	393	239	294	361	324	403	463	442	403	409	415	366	420
A/NK	1.26	1.21	1.18	1.33	1.14	1.17	1.29	1.35	1.17	1.31	1.31	1.34	1.38	1.16	1.36
A/CNK	1.07	1.09	1.14	0.95	0.97	1.04	1.02	1.13	1.01	1.12	1.13	1.11	1.07	1.00	1.06
DI	—	—	—	—	—	—	—	—	—	—	—	—	—	—	—
Nb/Ta	6.12	8.32	7.33	6.81	6.88	9.72	15.30	11.06	9.87	10.27	10.15	4.52	4.57	7.15	5.57
Zr/Hf	33.0	28.2	28.5	26.8	22.5	26.9	37.0	30.0	31.1	31.3	30.3	27.5	27.8	23.3	29.4
∑LREE	231	175	138	164	113	230	445	152	126	166	140	212	84.0	178	111
∑HREE	24.4	27.2	15.1	19.2	7.3	21.7	20.5	24.7	26.9	19.5	19.4	26.5	—	—	—
∑REE	256	202	153	184	121	252	465	176	153	185	160	239	—	—	—
δEu	0.38	0.22	0.27	0.46	0.60	0.17	0.21	0.20	0.24	0.21	0.24	0.18	0.38	0.19	0.43
δCe	1.02	0.97	0.83	0.96	1.02	0.96	1.03	0.99	0.98	1.01	0.99	0.96	0.86	0.86	0.85
1000*Ga/Al	2.68	2.69	2.49	2.33	2.17	2.69	2.85	2.55	2.73	2.76	2.65	2.72	3.09	2.83	2.35
Zr + Nb + Ce + Y	349	304	211	244	187	335	558	244	247	244	209	332	145	269	265
Rb/Sr	3.15	7.34	8.45	1.52	4.80	7.26	4.01	6.82	7.16	8.07	6.74	6.87	7.56	8.63	3.62
Rb/Nb	19.1	17.6	29.8	16.5	27.2	17.2	15.8	10.7	15.2	12.8	20.4	15.6	20.5	23.7	23.1
CaO/Na_2O	0.35	0.22	0.07	0.70	0.35	0.23	0.56	0.35	0.30	0.32	0.31	0.37	0.53	0.34	0.53
Rb/Ba	0.97	1.95	4.25	0.71	5.28	3.17	2.12	2.58	1.75	1.93	2.07	2.67	2.57	1.80	2.78
CaO + Al_2O_3	14.5	13.8	12.6	15.3	13.1	14.2	15.0	15.7	15.0	14.5	14.6	14.9	15.1	13.4	15.0
CaO/Al_2O_3	0.08	0.05	0.01	0.17	0.09	0.06	0.11	0.08	0.07	0.07	0.07	0.09	0.11	0.08	0.12
Y + Nb	60.3	68.8	35.8	41.9	21.4	47.5	44.6	76.7	74.9	63.6	49.7	68.8	33.3	51.5	41.2

No.	FG17-1[&]	FG18-1[&]	FG20-1[&]	FG-1[$]	FG-10[$]
	PBG (data from others)				
SiO_2	73.4	75.6	74.6	77.6	71.7
TiO_2	0.11	0.11	0.25	0.09	0.31
Al_2O_3	13.6	12.4	13.5	12.4	13.9

(Continued on the following page)

TABLE 3 (*Continued*) Major oxides (wt%) and trace element (ppm) compositions of representative samples from the Fogang granitic batholith[§].

No.	FG17-1[&]	FG18-1[&]	FG20-1[&]	FG-1[$]	FG-10[$]
	PBG (data from others)				
$Fe_2O_3^T$	1.02	1.38	1.92	0.73	2.46
MnO	0.04	0.03	0.07	0.07	0.05
MgO	0.28	0.16	0.39	0.00	0.47
CaO	1.56	0.96	1.56	0.37	1.46
Na_2O	2.95	2.85	2.97	3.82	2.59
K_2O	4.62	5.54	4.62	4.33	6.20
P_2O_5	0.21	0.02	0.09	0.02	0.10
LOI	2.03	0.63	0.53	0.36	0.91
Total	99.8	99.7	100.5	99.8	100.2
Ga	18.6	19.7	17.0	14.9	17.0
Rb	266	370	322	259	178
Sr	6.37	130	27.5	51.1	51.7
Y	22.6	32.4	37.5	28.3	23.7
Zr	98.8	241	174	109	156
Nb	22.7	18.8	21.1	21.2	12.3
Ba	35.5	880	95.4	132	276
La	34.6	101	39.2	19.5	42.1
Ce	55.9	153	79.6	41.0	71.1
Pr	6.82	17.5	10.6	4.58	7.67
Nd	21.6	64.5	46.9	17.6	26.2
Sm	4.04	11.0	12.5	4.52	4.82
Eu	0.24	1.16	0.43	0.44	0.59
Gd	4.15	11.0	10.3	4.74	4.40
Tb	—	—	—	0.75	0.63
Dy	—	—	—	5.12	4.20
Ho	—	—	—	1.11	0.91
Er	—	—	—	3.39	2.79
Tm	—	—	—	0.50	0.43
Yb	4.11	4.14	4.24	3.37	2.98
Lu	0.65	0.59	0.63	0.54	0.49
Hf	5.69	7.59	7.53	3.38	4.21

(Continued on the following page)

10.3389/feart.2025.1588243

TABLE 3 (*Continued*) Major oxides (wt%) and trace element (ppm) compositions of representative samples from the Fogang granitic batholith[§].

No.	FG17-1[&]	FG18-1[&]	FG20-1[&]	FG-1[$]	FG-10[$]
	PBG (data from others)				
Ta	3.20	3.85	2.68	2.39	1.62
Th	34.9	69.4	79.3	30.7	31.0
U	10.2	11.7	18.3	11.4	8.82
Ti	—	—	—	—	—
Pb	—	—	—	—	—
A/NK	1.13	1.27	1.27	1.25	1.22
A/CNK	1.06	1.02	1.05	1.02	1.02
DI	—	—	—	—	—
Nb/Ta	7.11	4.89	7.85	8.85	7.62
Zr/Hf	17.4	31.7	23.1	32.4	37.0
∑LREE	123	348	189	87.6	152
∑HREE	—	—	—	19.5	16.8
∑REE	—	—	—	107	169
δEu	0.18	0.32	0.12	0.29	0.39
δCe	0.89	0.90	0.96	1.06	0.97
1000*Ga/Al	2.83	2.67	2.61	2.22	2.28
Zr + Nb + Ce + Y	200	445	312	200	263
Rb/Sr	41.70	2.85	11.69	5.08	3.44
Rb/Nb	11.7	19.6	15.3	12.2	14.5
CaO/Na_2O	0.10	0.56	0.44	0.44	0.39
Rb/Ba	7.49	0.42	3.37	1.97	0.65
$CaO + Al_2O_3$	12.8	15.4	13.4	13.9	15.4
CaO/Al_2O_3	0.03	0.10	0.09	0.10	0.09
Y + Nb	45.4	51.3	58.5	49.5	36.0

[§] ACNK, molar $(Al_2O_3/(CaO + Na_2O + K_2O))$; A/NK, molar $[Al_2O_3/(Na_2O + K_2O)]$. "—" indicates missing data for this item.
#Data from Ding et al., 2022; *Data from Li et al., 2007; & Data from Chen et al., 2002; [$] Data from Ling et al., 2006.

diagram, distinct oxygen fugacity fields are delineated, allowing for the estimation of magmatic redox conditions. In the 1/T vs. δCe anomaly diagram (Figure 10), the PBG mainly falls in the region between the MH and FMQ fields, showing high oxygen fugacity with lg (fO_2) values ranging from −16.1 to −9.8 (mean = −13.2). The oxygen fugacity values of M-FG TMG and FG TMG are mainly below the FMQ region, with lg (fO_2) values ranging from −26.3 to −13.1 (mean = −20.2) and −28.6 to −7.8 (mean = −17.3), respectively, which are significantly lower than that of PBG.

6 Discussion

6.1 Geochronology

The LA-ICP-MS zircon U–Pb age of the PBG in the Pajiang area, located in the southwestern part of the Fogang granitic batholith, is 156.7 ± 0.7 Ma (MSWD = 0.2, n = 11). This is broadly consistent with the crystallization age of 158 ± 17 Ma (MSWD = 2.79, n = 5) obtained by Bao and Zhao (2003) using the Rb–Sr method,

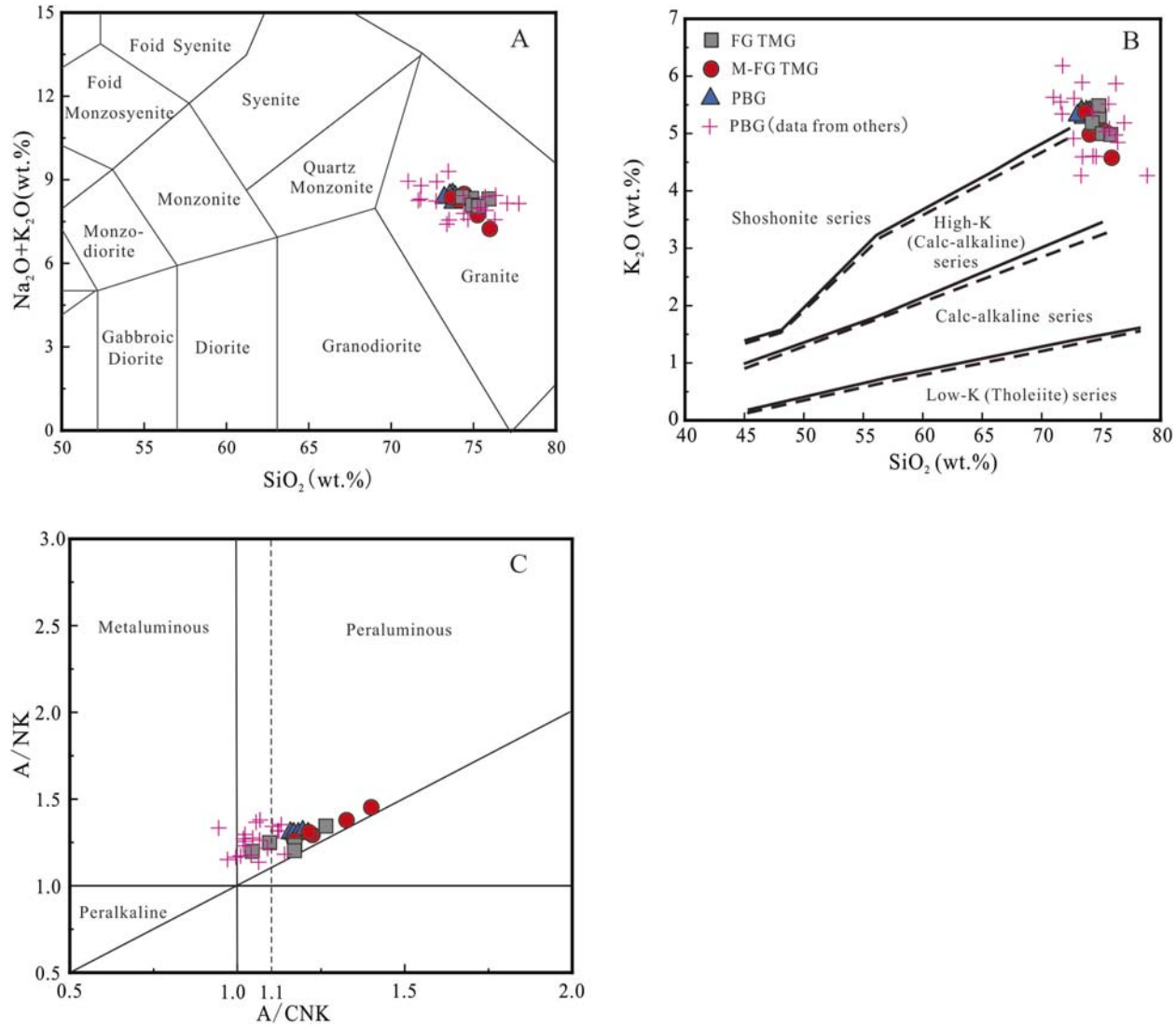

FIGURE 6
(A) SiO_2–(K_2O + Na_2O) diagram (bottom panel according to the study of Middlemost, 1994); **(B)** SiO_2–K_2O diagram (bottom panel according to the study of Middlemost, 1985); **(C)** A/CNK–A/NK diagram (bottom panel according to the study of Maniar and Piccoli, 1989). The data on the porphyritic biotite granite published by others are from Ding et al. (2022), Li et al. (2007), Chen et al. (2002), and Ling et al. (2006); see the data in Table 3.

which falls within analytical uncertainty and suggests that the Fogang granitic batholith is a product of early Yanshanian magmatic activity. Additionally, the LA-ICP-MS zircon U–Pb ages for the M-FG TMG and FG TMG are 155.3 ± 1.6 Ma (MSWD = 0.5, n = 12) and 153.8 ± 1.4 Ma (MSWD = 0.6, n = 24), respectively. These ages indicate that these granites formed during the early Yanshanian period and experienced multiple stages during the same period.

The Pajiang deposit is the only uranium deposit found in the Fogang granitic batholith. The LA-ICP-MS U–Pb dating result for the pitchblende in the deposit is 49.70 ± 0.1 Ma (MSWD = 0.16, n = 9) (Li et al., 2024b). A significant temporal discrepancy exists between the mineralization and the emplacement of the host rocks (PBG, M-FG TMG, and FG TMG), indicating that the deposit is of epigenetic hydrothermal origin. Additionally, the PBG is characterized by significant enrichment in uranium (average uranium content = 14.6 ppm) and thorium (average thorium content = 43.0 ppm). In contrast, the M-FG TMG and FG TMG exhibit higher uranium content (average 15.3 ppm) but lower thorium content (average 25.6 ppm), with Th/U ratios <3. The high U–Th characteristics of PBG may correlate with allanite (Figure 3C), which is in line with previous studies that reported significant allanite enrichment in these granites (Jayananda et al., 2000; Cuney, 2014). In contrast, the M-FG TMG and FG TMG exhibit elevated U but depleted Th contents and serve as the host rock for the Pajiang uranium deposit. It is inferred that uranium is probably present in more leachable uranium-bearing minerals, such as uraninite. Uraninite is more susceptible to leaching by later hydrothermal alteration, which could provide metallogenic material for subsequent uranium mineralization events (Qi et al., 2014; Qiu et al., 2018; Zhang et al., 2021b). This is consistent with the characteristics of granite-type uranium deposits in South

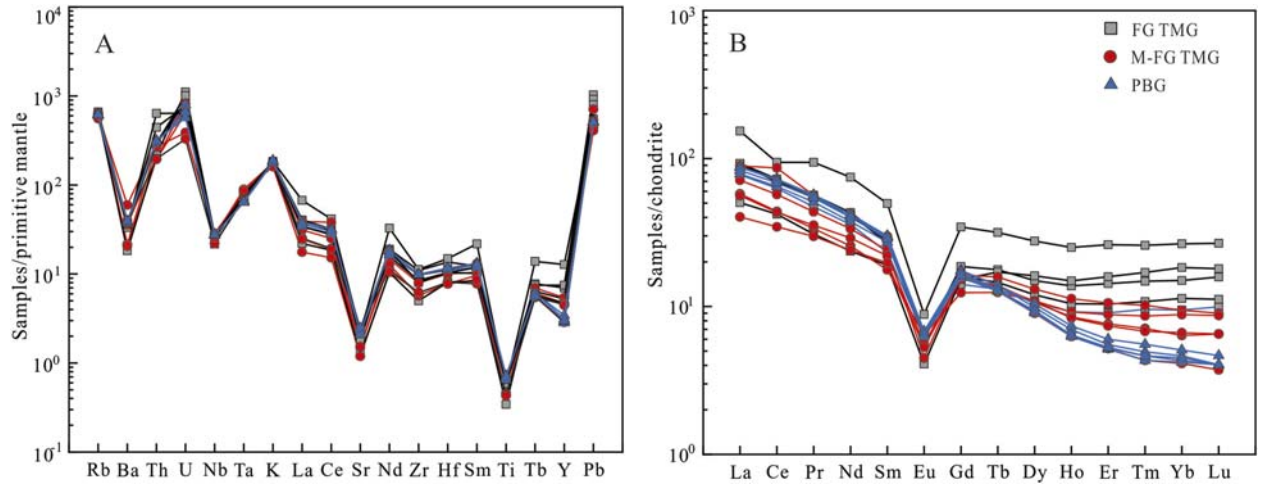

FIGURE 7
(A) Trace-element spider diagram and **(B)** chondrite-normalized REE patterns of granites in the Fogang granitic batholith. **(A)** Normalized data on the primitive mantle (standardized values according to the study of McDonough et al., 1991); **(B)** normalized data on chondrite (standardized values according to the study of Sun and McDonough, 1989).

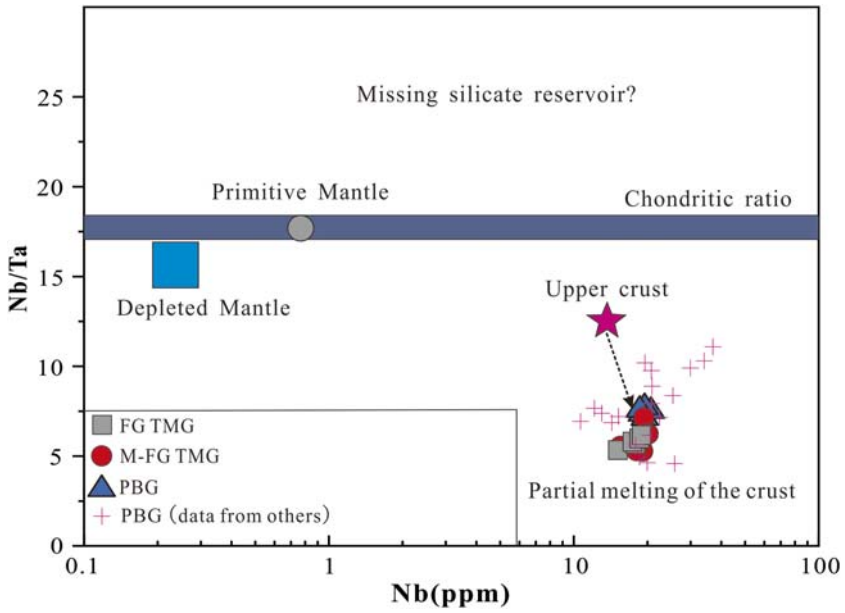

FIGURE 8
Plot of Nb vs. Nb/Ta (bottom panel according to the study of Barth et al., 2000). Other data sources are the same as detailed in Figure 6.

China, where mineralization typically postdates the formation of the host rocks (Zhang et al., 2021b).

6.2 Petrogenetic type

In the Harker diagram (Figure 11), the PBG, M-FG TMG, and FG TMG display a pronounced negative correlation between SiO_2 content and MgO, CaO, $Fe_2O_3^T$, and Na_2O, indicating a genetic relationship driven by magmatic evolution. The M-FG TMG and FG TMG exhibit higher differentiation indices (DI = 92.9–95.1) than the PBG (DI = 92.3–93.3). This geochemical trend, coupled with the elevated DI values, suggests that the M-FG TMG and FG TMG represent late-stage fractionated products derived from the parental magma. Given that magmatic differentiation significantly modifies the primary chemical composition, the geochemical characteristics of the M-FG TMG and FG TMG cannot be used to directly infer the original composition of the parent magma (Chen and Yang, 2015).

As a result, neither M-FG TMG nor FG TMG is appropriate for constraining the petrogenetic classification of the Fogang

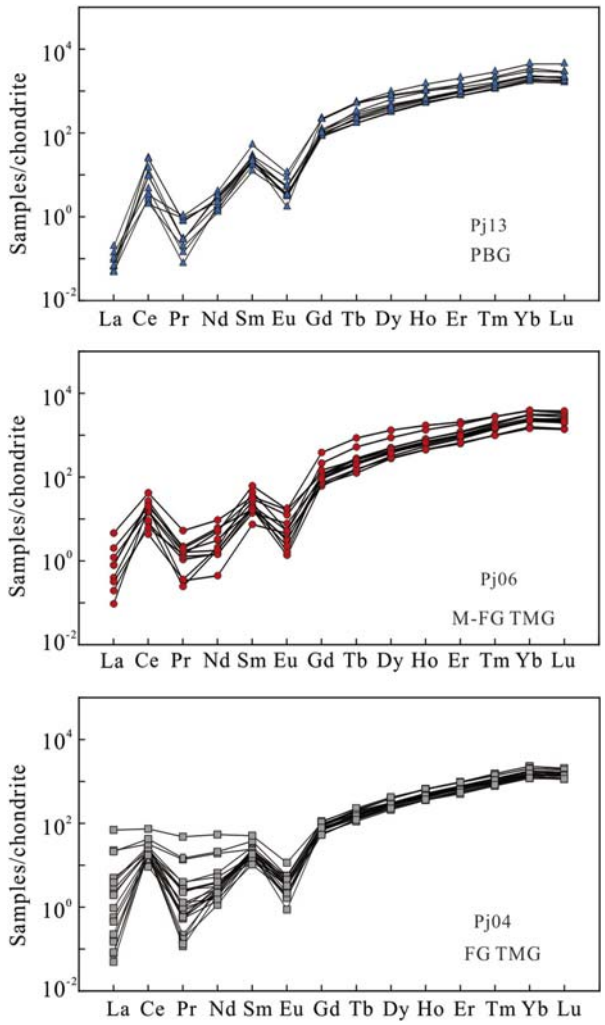

FIGURE 9
Chondrite-normalized REE patterns of zircons from the Fogang granitic batholith (standardized values according to the study of Sun and McDonough, 1989).

granitic batholith. Only PBG is viable for distinguishing the petrogenetic types of the Fogang granitic batholith. A-type granites are characterized by Zr + Nb + Ce + Y > 350 ppm and Zr > 250 ppm (Whalen et al., 1987). The Zr + Nb + Ce + Y and Zr contents of the PBG in the Fogang granitic batholith range from 88 to 349 ppm and from 75.5 to 241 ppm (except for sample No. 2KSC79*, F18-1), respectively, which are significantly lower than those of A-type granites. In the 10,000 Ga/Al versus Zr diagram, data points for the PBG fall within the overlapping field of A-type granites and highly fractionated I- and S-type granites (Figure 12A). However, the zircon crystallization temperatures of this granite range from 622 °C to 775 °C, with an average of 714 °C (Table 2), which is significantly lower than the mean temperature of A-type granites (839 °C, n = 55) reported by King et al. (1997). Moreover, the total REE concentrations in this granite range from 107 to 465 ppm, with an average of 183 ppm—substantially lower than those reported for Nanling A-type granites (ΣREE = 336–346 ppm) (Zhu et al., 2008). Additionally, the chondrite-normalized REE pattern of the studied granite differs markedly from that of typical A-type granites (Lan et al., 2020). Collectively, these geochemical characteristics suggest that the PBG does not represent an A-type granite but more likely corresponds to a highly fractionated I- or S-type granite (Figure 12B).

Petrogenetic discrimination studies by Chappell (1999) have shown that the covariation between P_2O_5 and SiO_2 in granites serves as a key geochemical indicator. Within his genetic classification framework, I-type granites typically display a pronounced negative correlation between P_2O_5 and SiO_2, reflecting magmatic fractionation processes. In contrast, S-type granites exhibit no significant correlation as apatite saturation in crustal melt–residue systems constrains phosphorus behavior. In the PBG from the Fogang granitic batholith, the analytical results reveal P_2O_5 contents ranging from 0.02 wt% to 0.21 wt% and SiO_2 contents ranging from 71.0 wt% to 77.6 wt%, with no statistically significant linear correlation observed ($R^2 = 0.13$). This geochemical signature aligns well with the diagnostic criteria for S-type granites, indicating a crustal origin through partial melting of metasedimentary protoliths. In the Rb versus Y diagram (Figure 12C), the majority of PBG samples plot within the evolutionary field characteristic of S-type granites. The zircons from these granites exhibit elevated Pb levels (60.7–360 ppm) and pronounced negative δEu anomalies (0.02–0.12) (Table 2), which are similar to the geochemical characteristics of zircons in typical S-type granites (Wang et al., 2012; Li et al., 2021). In the Pb vs. Th plot (Figure 12D), zircon data points are also present in the S-type granite field, which further proves that the PBG are highly fractionated "S"-type granites.

6.3 Origin of granitic magma

Previous studies have demonstrated that the enrichment levels of Rb, Sr, and Nb, along with their ratios in granitic rocks, are closely related to the nature of the source rock and thus serve as valuable indicators of magma origin.

The Rb/Sr and Rb/Nb ratios of the PBG, M-FG TMG, and FG TMG range from 1.52 to 41.7 and 10.7 to 29.8, respectively, both of which are significantly higher than the corresponding values for the upper continental crust (0.32 and 4.5, respectively), as reported by Taylor and McLennan (1995). These rocks may have originated from continental crust material with high maturity. Sylvester (1998) reported that the CaO/Na_2O ratios were lower than 0.30 when magma was derived from pelitic source rocks, whereas the CaO/Na_2O ratios were higher than 0.30 when magma was derived from clastic source rocks. The CaO/Na_2O ratios of the PBG range from 0.07 to 0.70; this broad range likely results from partial melting and mixing processes between pelitic and clastic source rocks. The CaO/Na_2O ratios of the FG TMG and M-FG TMG range from 0.06 to 0.29, with an average value of 0.14, which is lower than 0.30. This indicates that the source rocks of these two types of two-mica granites are mainly pelitic. In the Al_2O_3/TiO_2 vs. CaO/Na_2O (Figure 13A) and Rb/Sr vs. Rb/Ba (Figure 13B) bivariate plots, the data points of PBG are located in the mixed pelitic and clay-rich source areas, whereas those of M-FG TMG and FG TMG are mainly clustered in the pelitic source rock areas. These results imply that the source of PBG is a mixture of pelitic and clastic rocks,

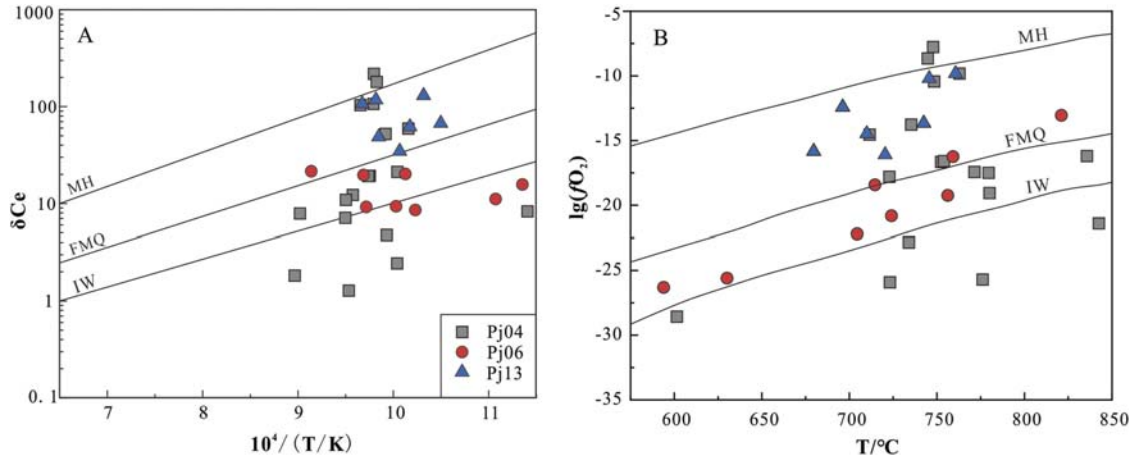

FIGURE 10
(A) Magma oxidation state diagram (bottom panel according to the study of Trail et al., 2011); **(B)** magma oxygen fugacity diagram (bottom panel according to the study of Trail et al., 2012). MH, magnetite–hematite; FMQ, fayalite–magnetite quartz; IW, iron–wuestite.

whereas the sources of M-FG TMG and FG TMG are predominantly pelitic rocks.

6.4 Tectonic setting

Intense magmatic activity occurred in South China after the Early Jurassic, resulting in multiple stages of tectonic deformation and the formation of large areas of granites, volcanic rocks, and mafic rocks (Mao et al., 2015; Ji et al., 2018; Zhang D. et al., 2018). Many geologists propose that lithosphere extension and thinning, coupled with asthenosphere upwelling, are the main mechanisms responsible for large-scale Mesozoic magmatism in South China (Li et al., 2007; Jiang et al., 2015; 2017; Wang et al., 2015; Xing et al., 2009).

Petrogenetic studies indicate that distinct magma series form in different tectonic environments: shoshonitic rocks typically develop in extensional settings, whereas high-K calc-alkaline magmas are genetically associated with post-collisional processes (Wang et al., 2019). The PBG, M-FG TMG, and FG TMG display transitional geochemical characteristics between high-K calc-alkaline and shoshonitic series, suggesting that their emplacement occurred within a post-collisional extensional regime. This interpretation is further supported by systematic geochemical discriminators, as shown in the Rb vs. Y + Nb and SiO_2 vs. Al_2O_3 tectonic setting diagrams (Figures 14A,B), where all analytical data from PBG, M-FG TMG, and FG TMG consistently plot within the post-collisional field.

Previous studies have demonstrated that the South China plate experienced post-orogenic extension during 160–150 Ma (Hua et al., 2005). Under these tectonic conditions, extensive magma ascent led to the formation of granitic bodies (Hua et al., 2005). The Fogang granitic batholith, comprising PBG, M-FG TMG, and FG TMG, formed during this period and is interpreted as a product of post-collisional extensional tectonics. Post-collisional extensional regime not only caused the formation of widespread granites but also exerted a significant influence on the spatial distribution and geochemical characteristics of uranium mineralization across the region. The lithospheric thinning and asthenospheric upwelling caused by the extensional stress likely played a crucial role in these processes, facilitating the partial melting of crustal materials and generating metaluminous to peraluminous felsic magmas. These magmas crystallized to form S-type granites, which became significant sources for subsequent uranium mineralization. This process may have subsequently been facilitated by tectonic events or regional stress field reorganizations that reactivated pre-existing fractures, creating preferential pathways for hydrothermal fluid migration and ultimately contributing to the genesis of uranium deposits.

6.5 Redox conditions of magmas and implications for uranium mineralization

Zircon trace and rare earth elements can be used to reveal the initial oxidation conditions and temperatures of magma due to their stable chemical properties, which remain unaltered during hydrothermal alteration (Green, 1995; Li et al., 2022). It has been proposed that Y/Ho ratios in zircon can be utilized to assess whether alteration by late-stage hydrothermal fluids has occurred (Zhang et al., 2011; Jiang et al., 2024). The Y/Ho ratios of the zircons from PBG, M-FG TMG, and FG TMG range from 26.5 to 31.3 (Table 2), which fall into the field without hydrothermal alteration (Y/Ho = 24–34), indicating that the zircons in the PBG, M-FG TMG, and FG TMG in this area were unaffected by hydrothermal fluids after their crystallization. Therefore, the oxygen fugacity recorded in zircon grains can serve as a reliable proxy for the whole-rock oxygen fugacity of granites.

Existing studies indicate that magmatic oxygen fugacity is generally insufficient to stabilize uranium in the hexavalent state (U^{6+}), with uranium predominantly occurring as tetravalent U^{4+}. During the early stages of magmatic evolution, U^{4+} exhibits a weaker oxygen-binding capacity than Si and Al, owing to its lower ionic potential (Chen et al., 2009). Consequently, the

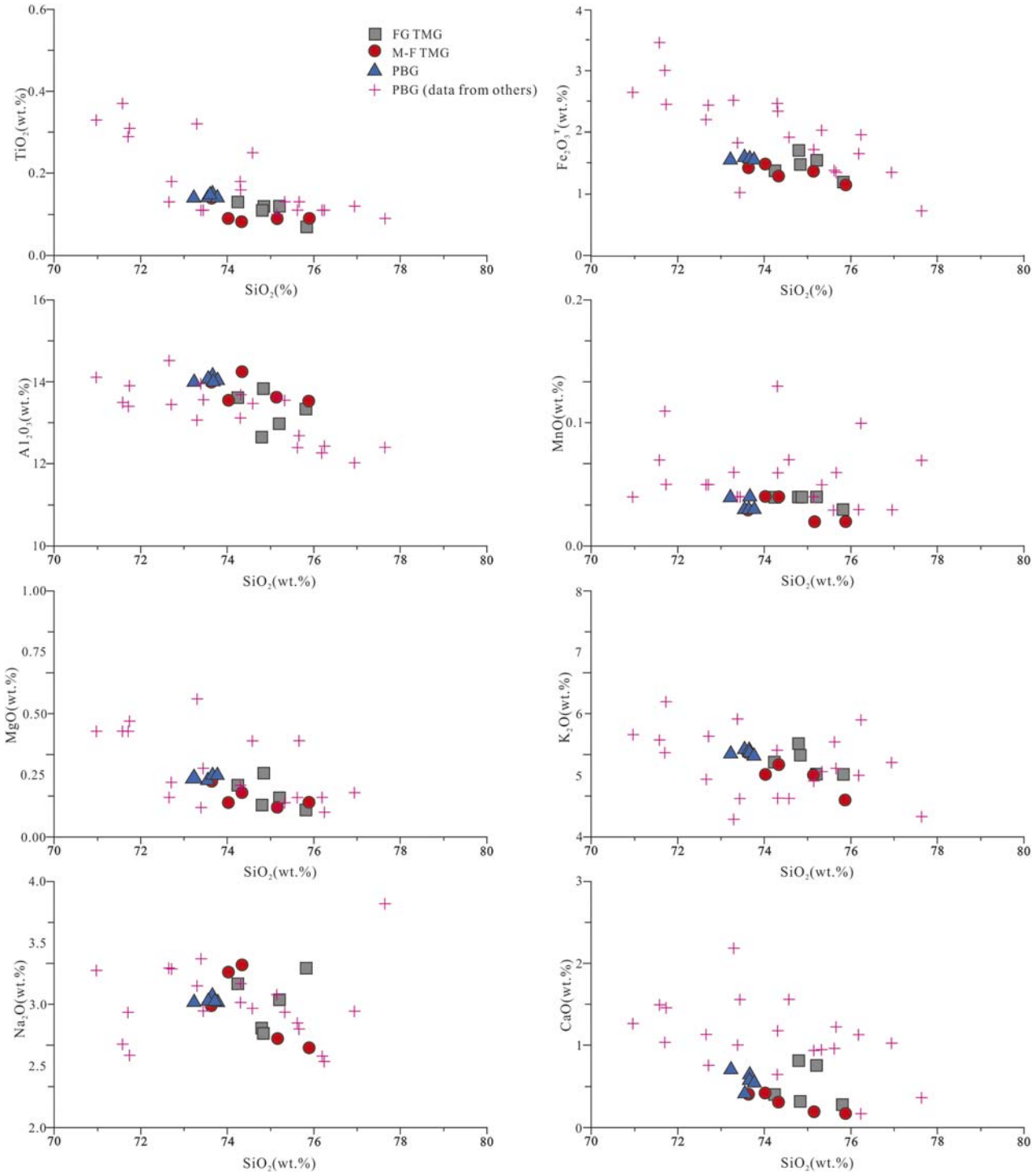

FIGURE 11
Harker diagram of the Fogang granitic batholith. Other data sources are the same as detailed in Figure 6.

formation of uranium oxides is limited, and uranium tends instead to associate with Th^{4+}, Zr^{4+}, and Y^{3+} to form uranium-bearing accessory minerals, such as monazite, thorite, and zircon. These accessory minerals are notably resistant to alteration during subsequent hydrothermal processes (Hu et al., 2012; Qi et al., 2014; Zhang et al., 2022; Xu et al., 2023).

Progressive magmatic evolution into the middle to late stages induces compositional changes characterized by decreasing temperature and oxygen fugacity, accompanied by increasingly reducing conditions and reduced isomorphous substitution. The consumption of REEs during earlier accessory mineral crystallization establishes geochemical conditions favorable for

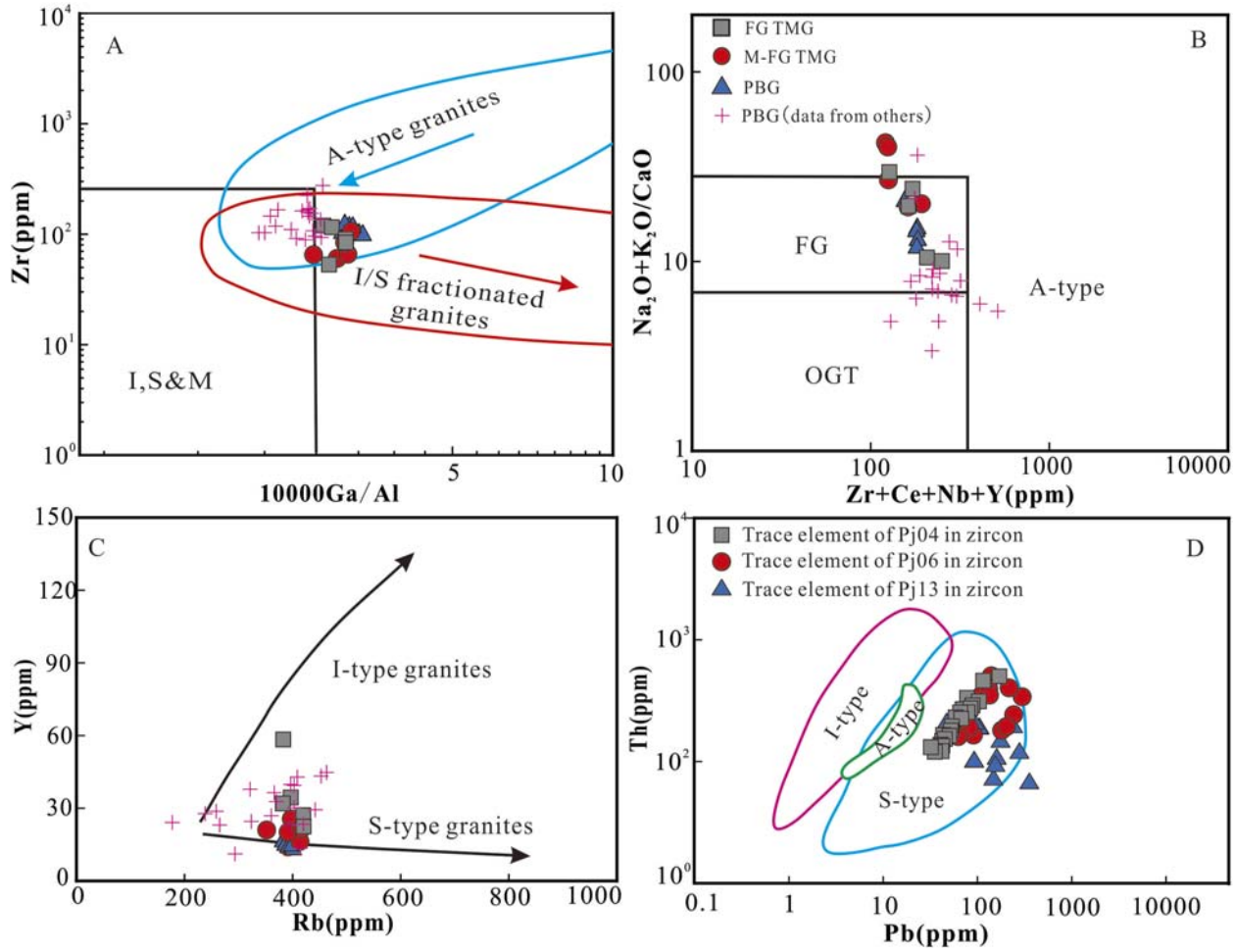

FIGURE 12
(A) Plot of 10000Ga/Al vs. Zr (bottom panel from the study of Wu et al., 2023); **(B)** plot of Zr + Nb + Ce + Y vs. (K_2O+ Na_2O)/CaO (bottom panel from the study of Whalen et al., 1987); **(C)** Plot of the Rb vs. Y diagram (bottom panel from the study of Chappell, 1999); **(D)** plot of the Pb vs. Th diagram for zircon (bottom panel from the study of Wang et al., 2012). Other data sources are the same as detailed in Figure 6.

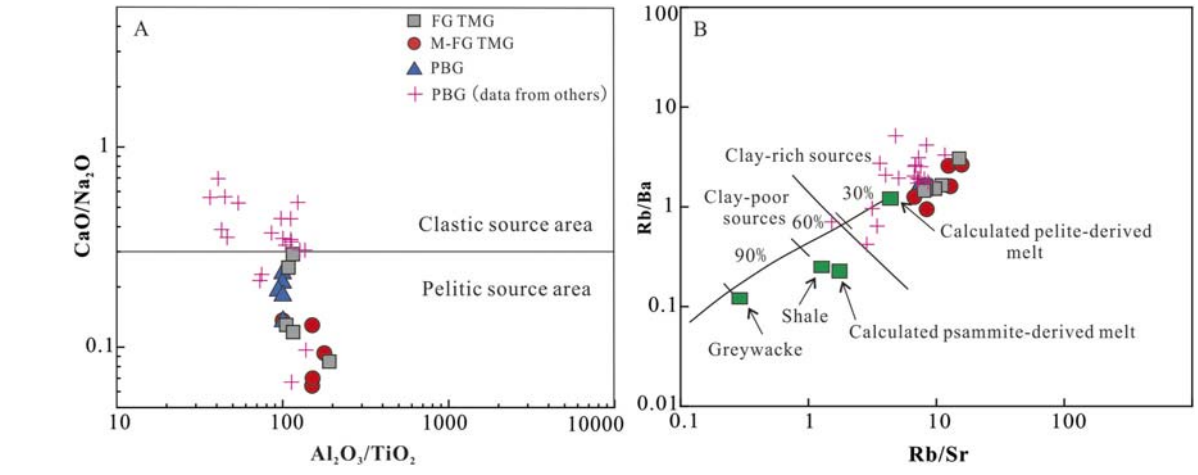

FIGURE 13
(A) Plot of CaO/Na_2O vs. Al_2O_3/TiO_2 (bottom panel according to the study of Sylvester, 1998); **(B)** plot of Rb/Sr vs. Rb/Ba (bottom panel according to the study of Sylvester, 1998). Other data sources are the same as detailed in Figure 6.

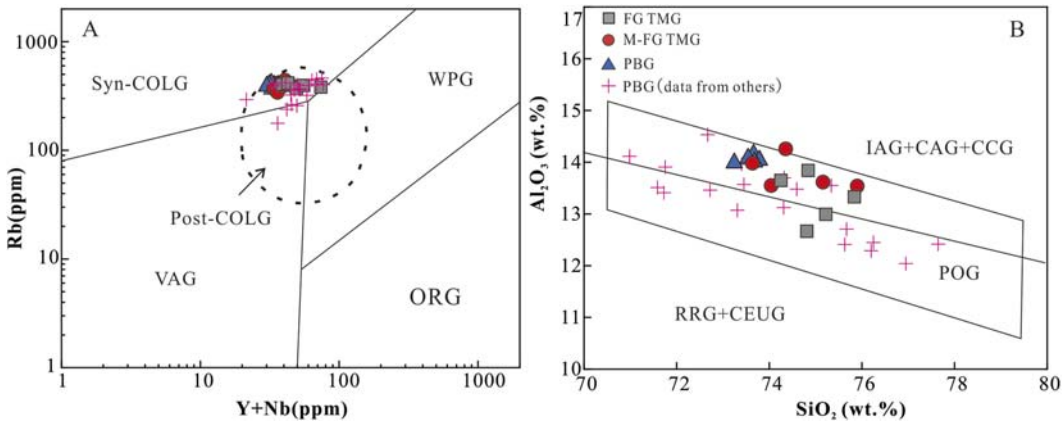

FIGURE 14
(A) Plot of Y + Nb vs. Rb (bottom panel according to Pearce, 1996); **(B)** plot of SiO_2 vs. Al_2O_3 (bottom panel according to Maniar and Piccoli, 1989). Syn-COLG, syn-collisional granite; WPG, within-plate granite; VAG, volcanic arc granite; ORG, ocean ridge granite; Post-COLG, post-collisional granites; IAG, island arc granitoid; CAG, continental arc granitoid; CCG, continental collision granitoid; POG, post-orogenic granitoid; RRG, rift-related granitoid; CEUG, continental epeirogenic uplift granitoid. Other data sources are the same as detailed in Figure 6.

uranium–oxygen bonding, ultimately leading to the precipitation of uraninite. Crystalline uranium minerals are highly susceptible to alteration by late-stage fluids, which promotes the release of uranium into these fluids, enabling its accumulation and creating favorable conditions for subsequent uranium mineralization (Zhang et al., 2022).

As previously noted, the oxygen fugacity of PBG (lg fO_2 = −16.1 to −9.8, with an average of −13.2) is significantly higher than that of M-FG TMG and FG TMG (lg fO_2 = −28.6 to −7.8, averaging −18.2). This trend indicates that, as the magma evolved from PBG to M-FG TMG and FG TMG, its oxygen fugacity decreased, thereby promoting the crystallization of uranium in two-mica granites in the form of uraninite. Furthermore, the uranium content in two-mica granites (15.3 ppm) is 0.7 ppm higher than that in PBG (14.6 ppm). The combination of lower oxidation states and higher uranium enrichment in two-mica granites suggests that they likely represent the primary uranium source rocks for the Pajiang uranium deposit. This interpretation is consistent with the prevailing view that two-mica granites constitute major uranium source rocks for granite-type uranium deposits in South China (Li et al., 2023; Tao et al., 2025). Therefore, regions containing two-mica granites should be prioritized in future exploration efforts targeting granite-type uranium mineralization.

7 Conclusion

Based on the major oxide and trace element compositions, ages, and zircon trace-element data of the porphyritic biotite granite and two-mica granites, the following conclusions are drawn:

1. The rock-forming ages of the PBG, M-FG TMG, and FG TMG, as determined by LA-ICP-MS zircon U–Pb dating, are 156.7 ± 0.7 Ma, 155.3 ± 1.6 Ma, and 153.8 ± 1.4 Ma, respectively, indicating a single magmatic event.
2. The PBG of the Fogang granitic batholith features high silicon, alkali, potassium, and aluminum supersaturation; a high fractionation index; low REE contents; and high Rb/Sr ratios, which are characteristic of highly fractionated S-type granites. The source rocks of PBG are a mixture of pelitic and clastic rocks, whereas those of M-FG TMG and FG TMG are pelitic rocks.
3. The oxygen fugacity is the highest in the PBG of the Pajiang area, followed by the M-FG TMG, with the FG TMG exhibiting the lowest values. The M-FG TMG and FG TMG represent potential uranium source rocks. Two-mica granites should be prioritized in future exploration efforts targeting granite-type uranium mineralization.
4. The granites in the Pajiang area, including PBG, M-FG TMG, and FG TMG, are classified as high-K calc-alkaline granites. Their formation is predominantly attributed to post-collisional extensional tectonics.

Data availability statement

The datasets presented in this study can be found in online repositories. The names of the repository/repositories and accession number(s) can be found in the article/supplementary material.

Author contributions

PH: Data curation, Formal Analysis, Investigation, Writing – original draft. W-CD: Conceptualization, Funding acquisition, Project administration, Writing – review and editing. BL: Conceptualization, Data curation, Formal Analysis, Investigation, Writing – review and editing. W-FW: Data curation, Formal Analysis, Investigation, Writing – review and editing. J-MQ: Investigation, Software, Writing – review and editing. LQ: Data curation, Investigation, Methodology, Writing – review and editing.

Funding

The author(s) declare that financial support was received for the research and/or publication of this article. This study was supported by the National Natural Science Foundation of China (Grant No. 42372263), the "Revelation and Command" project of the Natural Uranium Industry Technology Innovation Consortium (Grant No. 202303), and the Open Fund of the Shanghai Sheshan National Field Scientific Observation and Research Station of Geophysics (Grant No. SSOP202401).

Acknowledgments

The authors are grateful to Prof. Hao Song, Chengdu University of technology, for his valuable suggestions and assistance during the preparation of this manuscript.

Conflict of interest

Authors PH, BL, and J-MQ were employed by Research Institute No. 290, China National Nuclear Corporation. Author WW was employed by Research Institute of Shaanxi Yanchang Petroleum (Group) Co., Ltd.

The remaining authors declare that the research was conducted in the absence of any commercial or financial relationships that could be construed as a potential conflict of interest.

Generative AI statement

The author(s) declare that no Generative AI was used in the creation of this manuscript.

Any alternative text (alt text) provided alongside figures in this article has been generated by Frontiers with the support of artificial intelligence and reasonable efforts have been made to ensure accuracy, including review by the authors wherever possible. If you identify any issues, please contact us.

Publisher's note

References

Ballard, J. R., Palin, M. J., and Campbell, I. H. (2002). Relative oxidation states of magmas inferred from Ce (IV)/Ce (III) in zircon: application to porphyry copper deposits of Northern Chile. *Contrib. Mineral. petrol.* 144 (3), 347–364. doi:10.1007/s00410-002-0402-5

Bao, Z. W., and Zhao, Z. H. (2003). Geochemistry and tectonic setting of the Fogang aluminous A-type granite, Guangdong province, China- A preliminary study. *Geol. – Geochem (Guiyang, China)* 31 (1), 52–61. doi:10.3969/j.issn.1672-9250.2003.01.009

Barth, M. G., McDonough, W. F., and Rndnick, R. L. (2000). Tracking the budget of Nb and Ta in the continental crust. *Chem. Geol.* 165, 197–213. doi:10.1016/S0009-2541(99)00173-4

Chabiron, A., Cuney, M., and Poty, B. (2003). Possible uranium sources for the largest uranium district associated with volcanism: the Streltsovka caldera (Transbaikalia, Russia). *Min. Depos.* 38, 127–140. doi:10.1007/s00126-002-0289-0

Chappell, B. W. (1999). Aluminium saturation in I- and S-type granites and the characterization of fractionated haplogranites. *Lithos* 46, 535–551. doi:10.1016/S0024-4937(98)00086-3

Chen, J. Y., and Yang, J. H. (2015). Petrogenesis of the Fogang highly fractionated I-type granitoids: constraints from Nb, Ta, Zr and Hf. *Acta Petrol. Sin.* 31 (3), 846–854.

Chen, X. M., Wang, R. C., Liu, C. S., Hu, H., Zhang, W. L., and Gao, J. F. (2002). Isotopic dating and genesis for Fogang biotite granites of Conghua area, Guangdong Province. *Geol. J. China Univ.* 8, 293–307. doi:10.16108/j.issn1006-7493.2002.03.006

Chen, Y. W., Bi, X. W., Hu, R. Z., and Qi, H. W. (2009). Comparison of geochemical characteristic of uranium and non-uranium-bearing indosinian granites in Guidong composite pluton. *J. Mineral. Petrol.* 29, 106–114. doi:10.1360/972008-2143

Cuney, M. (2009). The extreme diversity of uranium deposits. *Min. Depos.* 44, 3–9. doi:10.1007/s00126-008-0223-1

Cuney, M. (2014). Felsic magmatism and uranium deposits. *Bull. Soc. Geol. Fr.* 185 (2), 75–92. doi:10.2113/gssgfbull.185.2.75

Ding, X., Su, K. L., Yan, H. B., Liang, J. L., and Sun, W. D. (2022). Effect of F-rich fluids on the A-type magmatism and related metal mobilization: new insights from the Fogang-Nankunshan-Yajishan igneous rocks in southeast China. *J. Earth Sci.* 33 (3), 591–608. doi:10.1007/s12583-022-1611-7

Fan, H. H., Pang, Y. Q., He, D. B., Chen, D. H., Wang, Y. J., Sun, Y. Q., et al. (2023). Metallogenic process and prediction of granite-related uranium deposits in south China. *Acta Geosci. Sin.* 44 (5), 887–896. doi:10.3975/cagsb.2022.12210

Ferry, J. M., and Watson, E. B. (2007). New thermodynamic models and revised calibrations for the Ti-in-zircon and Zr-in-rutile thermometers. *Contrib. Mineral. Petrol.* 154 (4), 429–437. doi:10.1007/s00410-007-0201-0

Gao, J. F., Ling, H. F., Sheng, W. Z., Lu, J. J., Zhang, M., Huang, G. L., et al. (2005). Geochemistry and petrogenesis of Lianyang granite composite, west Guangdong province. *Acta Petrol. Sin.* 21 (6), 1645–1656.

Green, T. H. (1995). Significance of Nb/Ta as an indicator of geochemical processes in the crust mantle system. *Chem. Geol.* 120, 347–359. doi:10.1016/0009-2541(94)00145-X

Guangdong Bureau of geology and mineral resources, Team No.705 (1983). Geological survey and evaluation report on uranium deposits in the Shengping-Longshan segment of the Fogang No.261 area, Qingyuan, Guangdong Province, China (Unpublished report).

Guo, M., and Huang, K. W. (2019). Geochemistry, chronology and geological significance of medium grain porphyritic granite in the Fogang intrusion, northern Guangdong. *Geol. Min. Resour. South China* 35 (2), 158–170. doi:10.3969/j.issn.1007-3701.2019.02.003

Hu, H., Wang, R. C., Chen, W. F., Ding, H. H., Chen, P. R., and Ling, H. F. (2012). Study on uranium resource minerals of Douzhashan uranium-bearing granite, Northeastern Guangxi. *Geol. Rev.* 58 (6), 1056–1068. doi:10.16509/j.georeview.2012.06.002

Hu, Z. C., Zhang, W., Liu, Y. S., Gao, S., Li, M., Zong, K. Q., et al. (2015). The assembly of Rodinia: the correlation of early Neoproterozoic (ca.900 Ma) high-grade metamorphism and continental arc formation in the southern Beishan Orogen, southern Central Asian Orogenic Belt (CAOB). *Precambrian Res.* 290, 32–48. doi:10.1016/j.precamres.2016.12.010

Hua, R. M., Chen, P. R., Zhang, W. L., Yao, J. M., Lin, J. F., Zhang, Z. S., et al. (2005). Metallogeneses and their geodynamic settings related to Mesozoic granitoids in the Nanling range. *Geol. J. China Univ.* 11 (3), 291–304. doi:10.3969/j.issn.1006-7493.2005.03.002

Jayananda, M., Moyen, J. F., Martin, H., Peucat, J.-J., Auvray, B., and Mahabalesawar, B. (2000). Late Archaean (2550-2520 Ma) juvenile magmatism in the eastern Dharwar craton, southern India: constraints from geochronology, Nd-Sr isotopes and whole rock geochemistry. *Precamb. Res.* 99, 225–254. doi:10.1016/S0301-9268(99)00063-7

Ji, W. B., Chen, Y., Chen, K., Wei, W., Faure, M., and Lin, W. (2018). Multiple emplacement and exhumation history of the late mesozoic dayunshan-mufushan batholith in southeast China and its tectonic significance: 2. Magnetic fabrics and gravity survey. *J. Geophys. Res. Solid Earth* 123, 711–731. doi:10.1002/2017JB014598

Jiang, Y. H., Wang, G. C., Liu, Z., Ni, C. Y., Qing, L., and Zhang, Q. (2015). Repeated slab advance–retreat of the Palaeo-Pacific plate underneath SE China. *Int. Geol. Rev.* 57 (4), 472–491. doi:10.1080/00206814.2015.1017775

Jiang, Y. H., Wang, G. C., Qing, L., Zhu, S. Q., and Ni, C. Y. (2017). Early jurassic A-type granites in southeast China: shallow dehydration melting of early paleozoic granitoids by basaltic magma intraplating. *J. Geol.* 125 (3), 351–366. doi:10.1086/691242

Jiang, K. N., Luo, J. C., Zhong, F. J., Liu, G. Q., Zhang, X. T., and Jiang, X. Y. (2024). Zircon oxygen fugacity as a tracer to distinguish the parent rock volcanic-hosted uranium mineralization in the Xiangshan area, South China. *Acta Geol. Sin.* 98 (1), 181–199. doi:10.19762/j.cnki.dizhixuebao.2023019

King, P. L., White, A. J. R., Chappell, B. W., and Allen, C. M. (1997). Characterization and origin of aluminous A-type granites from the lachlan fold belt, southeastern Australia. *J. Petrol.* 38 (3), 371–391. doi:10.1093/petroj/38.3.371

Lan, H. F., Wang, H. Z., Ling, H. F., Chen, W. F., Wang, K. X., and Wang, D. (2020). Petrogenesis of the Chashan granite in the northern Guangdong province and its implication for the metallogenic potential of tungsten and uranium mineralization. *Acta Geol. sin.* 94 (4), 1143–1165.

Li, X. H., Li, Z. X., Liu, Y., Yuan, C., Wei, G. J., Qi, C. S., et al. (2007). U-Pb zircon, geochemical and Sr-Nd-Hf isotopic constraints on age and origin of Jurassic I-and A-type granites from central Guangdong, SE China: a major igneous event in response to foundering of a subducted flat-slab? *Lithos* 96, 186–204. doi:10.1016/j.lithos.2006.09.018

Li, H., Watanabe, K., and Yonezu, K. (2014). Zircon morphology, geochronology and trace element geochemistry of the granites from the Huangshaping polymetallic deposit, South China: implications for the magmatic evolution and mineralization processes. *Ore Geol. Rev.* 60, 14–35. doi:10.1016/j.oregeorev.2013.12.009

Li, J., Huang, H. Y., Liu, Z. J., Zhang, T., Wang, Q. L., Fang, S. Y., et al. (2021). La-ICP-MS U-Pb ages and trace element compositions of zircon from indosinian granites in middle Zhuguangshan. *Geotecton. Metallog.* 45 (6), 1216–1232. doi:10.16539/j.ddgzyckx.2021.06.007

Li, S. K., Liu, X. L., Lu, Y. X., Zhang, S. T., Liu, S. H., Chen, J. H., et al. (2022). Indication of zircon oxygen fugacity to different mineralization control factors of porphyry deposits in Zhongdian ore-concentrated area, Southern Yidun Arc. *Earth Sci.* 47 (04), 1435–1458. doi:10.3799/dqkx.2021.079

Li, K., Chen, W. F., Gao, S., Shen, W. Z., Huang, G. L., Liu, W. Q., et al. (2023). The petrogenesis of Baishuizhai granitic pluton and its significance to uranium mineralization in the Xiazhuang area, Guangdong province[J]. *Geol. J. China Univ.* 29 (4), 497–513. doi.doi:10.16108/j.issn1006-7493.2021117

Li, H. D., Jiang, W. B., Liu, B., Lai, J., and Guo, X. W. (2024a). Geological characteristics and prospecting potential of uranium mineralization in the south of Zhuguang pluton. *Uran. Geol.* 40 (3), 442–458. doi:10.3969/j.issn.1000-0658.2024.40.039

Li, H. D., Tian, S. H., Liu, B., Hu, P., Wu, J. Y., and Chen, Z. L. (2024b). *In-situ* microchronology and elemental analysis of pitchblende in the Pajiang uranium deposit, northern Guangdong: implication for uranium mineralization. *Earth Sci. Front.* 31 (2), 270–283. doi:10.13745/j.esf.sf.2023.11.70

Ling, H. F., Shen, W. Z., Sun, T., Jiang, S. Y., Jiang, Y. H., Ni, P., et al. (2006). Genesis and source characteristics of 22 Yanshanian granites in Guangdong province: study of element and Nd-Sr isotopes. *Acta Petrol. Sin.* 22 (11), 2687–2703.

Ludwig, K. R. (2003). *Isoplot 3.0: a geochronological toolkit for microsoft excel*. California, Berkeley: Berkeley Geochronology Center, 39.

Maniar, P. D., and Piccoli, P. M. (1989). Tectonic discrimination of granitoids. *Geol. Soc. Am. Bull.* 101 (5), 635–643. doi:10.1130/0016-7606(1989)101<0635:TDOG>2.3.CO;2

Mao, J. R., Li, Z. L., and Ye, H. M. (2015). Mesozoic tectono-magmatic activities in South China: retrospect and prospect. *Sci. China Earth Sci.* 57 (12), 2853–2877. doi:10.1007/s11430-014-5006-1

Mcdonough, W. F., Sun, S. S., Ringwood, A. E., Jagoutz, E., and Hoffmann, A. W. K. (1991). K, Rb and Cs in the earth and moon and the evolution of the earth's mantle. *Geochim. Cosmochim. Acta.*, 68–76. doi:10.1016/0016-7037(92)90043-I

Middlemost, E. A. K. (1985). *Magmas and magmatic rocks: an introduction to igneous petrology*. London: Longman, 1–226. doi:10.1180/minmag.1986.050.355.34

Middlemost, E. A. K. (1994). Naming materials in the magma/igneous rock system. *Earth-Sci. Rev.* 37 (3-4), 215–224. doi:10.1016/0012-8252(94)90029-9

Pearce, J. A. (1996). Sources and settings of granitic rocks. *Episodes* 19 (4), 120–125. doi:10.18814/epiiugs/1996/v19i4/005

Qi, J. M., Huang, G. L., Zhu, B., Fu, S. C., Xu, Y., and Ye, S. X. (2014). Compositions study of auxiliary minerals in altered granitic rocks of the Mianhuakeng uranium deposit in Northern Guangdong. *Acta Geol. Sin.* 88 (9), 1691–1704. doi:10.19762/j.cnki.dizhixuebao.2014.09.006

Qiu, L., Yan, D. P., Tang, S. L., Arndt, N. T., Fan, L. T., Guo, Q. Y., et al. (2015). Cooling and exhumation of the oldest Sanqiliu uranium ore system in Motianling district, South China Block. *Terra nova.* 27 (6), 449–457. doi:10.1111/ter.12179

Qiu, L., Yan, D. P., Ren, M., Cao, W., Tang, S. L., Guo, Q. Y., et al. (2018). The source of uranium within hydrothermal uranium deposits of the Motianling mining district, Guangxi, South China. *Ore Geol. Rev.* 96, 201–217. doi:10.1016/j.oregeorev.2018.04.001

Shu, L. S., Zhou, X. M., Deng, P., and Yu, X. Q. (2006). Principal geological features of Nanling tectonic belt, South China. *Geol. Rev.* 52, 251–265. doi:10.1016/S1001-8042(06)60011-0

Sun, X. S., and Mcdonough, W. F. (1989). "Chemical and isotopic systematics of oceanic basalts: implications for mantle composition and processes," *Isotopic Syst. Ocean. basalts Implic. mantle Compos. Process.* (London: Geological Society), 42. 313–345. doi:10.1144/GSL.SP.1989.042.01.19

Sylvester, P. J. (1998). Post-collisional strongly peraluminous granites. *Lithos* 45, 29–44. doi:10.1016/S0024-4937(98)00024-3

Tao, J. H., Yang, Y. G., Su, X. Y., Leng, C. B., Li, K. X., Chen, X. L., et al. (2025). Petrogenesis of U-rich two-mica granite from the Mesozoic Reshui pluton (Nanling Range, South China) with implications for uranium mineralization. *J. Asian Earth Sci.* 277, 106400. doi:10.1016/j.jseaes.2024.106400

Taylor, S. R., and McLennan, S. M. (1995). The geochemical evolution of the continental crust. *Rev. Geophys.* 33 (2), 241–265. doi:10.1029/95RG00262

Trail, D., Watson, E. B., and Tailby, N. D. (2011). The oxidation state of Hadean magmas and implications for early Earth's atmosphere. *Nature* 480, 79–82. doi:10.1038/nature10655

Trail, D., Watson, E. B., and Tailby, N. D. (2012). Ce and Eu anomalies in zircon as proxies for the oxidation state of magmas. *Geochim. Cosmochim. Acta.* 97, 70–87. doi:10.1016/j.gca.2012.08.032

Wang, Q., Zhu, D. C., Zhao, Z. D., Guan, Q., Zhang, X. Q., Sui, Q. L., et al. (2012). Magmatic zircons from I-S- and A-type granitoids in Tibet: trace element characteristics and their application to detrital zircon provenance study. *J. Asian Earth Sci.* 53, 59–66. doi:10.1016/j.jseaes.2011.07.027

Wang, L. X., Ma, C. Q., Lai, Z. X., Marks, M. A. W., Zhang, C., and Zhong, Y. F. (2015). Early Jurassic mafic dykes from the Xiazhuang ore district (South China): implications for tectonic evolution and uranium metallogenesis. *Lithos* 239, 71–85. doi:10.1016/j.lithos.2015.10.008

Wang, T., Guo, L., Li, S., Wang, X. X., and Wang, C. Y. (2019). Some important issues in the study of granite tectonics. *J. Geomech.* 25 (5), 899–919. doi:10.12090/j.issn.1006-6616.2019.25.05.074

Whalen, J. B., Carrie, K. L., and Chappell, B. W. (1987). A-type granites: geochemical characteristics, discrimination and petrogenesis. *Contrib. Mineral. Petrol.* 95, 407–417. doi:10.1007/BF00402202

Wu, F. Y., Guo, C. L., Hu, F. Y., Liu, X. C., Zhao, J. X., Li, X. F., et al. (2023). Petrogenesis of the highly fractionated granites and their mineralizations in Nanling range, South China. *Acta Petrol. Sin.* 39 (01), 1–36. doi:10.18654/1000-0569/2023.01.01

Xin, H. B., and Qu, X. M. (2008). Relative oxidation states of ore-bearing porphyries inferred from Ce(IV)/Ce(III) ratio in zircon: application to the porphyry copper belt at Gangdese, Tibet. *Acta Mineral. Sin.* 28 (2), 152–160.

Xing, J. S., Yang, W. R., Xing, Z. Y., Liu, J. H., and Shao, J. S. (2009). Meso-Cenozoic asthenosphere upwelling of eastern China and its impacts on structure-magma-mineralization concentration region. *Earth Sci. Front.* 16 (4), 225–239. doi:10.1016/S1874-8651(10)60080-4

Xu, L. L. (2024). Fault characteristics and uranium prospecting direction in Pajiang area of Fogang pluton in northern Guangdong. *Uran. Geol.* 40 (3), 428–441. doi:10.3969/j.issn.1000-0658.2024.40.038

Xu, X. S., Lu, W. M., and He, Z. Y. (2007). Age and generation of Fogang granite batholith and Wushi diorite-horblende gabbro body. *Sci. China Earth Sci.* 37 (1), 27–38. doi:10.1007/s11430-007-2068-3

Xu, W. T., Zhang, X. H., Zhang, B. B., Lv, J. S., Sun, J. D., Zhang, Y., et al. (2022). Genesis of highly fractionated S-type granites: evidence from zircon U-Pb geochronology, Hf isotopes and geochemistry of Fuquanshan pluton, northeastern Jiangxi province. *Geol. Bull. China.* 41, 577–589. doi:10.12097/j.issn.167-2552.2022.04.005

Xu, P. L., Tang, X. S., Guo, F. S., Lv, C., Li, G. R., Dang, F. P., et al. (2023). Characteristics and geological significance of chorite from the cataclastic alteration granite-type uranium deposit in Lujing ore field, south China: perspective from Xiaoshan deposit. *Acta Geol. Sin.* 97 (2), 1211–1227. doi:10.19762/j.cnki.dizhixuebao.2023221

Yang, F., Han, H. W., Bian, T. Y., Yuan, X. J., Guo, X. F., Zou, D. H., et al. (2024). Identification of zircons of different origin in complex rock mass and its implications for zircon U-Pb age: a case study from zircon of Archean basement in Liaohe Depression. *Chin. J. Geol.* 59 (5), 1308–1325. doi:10.12017/dzkx.2024.092

Zhang, H., Sun, W. D., and Yang, X. Y. (2011). Chronology and metallogenic mechanism of the shapinggou super large porphyry Molybdenum deposit in the Dabie orogenic belt. *Acta Geol. Sin.* 85 (12), 2039–2059.

Zhang, L., Chen, Z. Y., Li, X. F., Li, S. R., Santosh, M., and Huang, G. L. (2018a). Zircon U-Pb geochronology and geochemistry of granites in the Zhuguangshan complex, South China: implications for uranium mineralization. *Lithos* 308-309, 19–33. doi:10.1016/j.lithos.2018.03.012

Zhang, D., Zhao, K. D., Chen, W., and Jiang, S. Y. (2018b). Early Jurassic mafic dykes from the Aigao uranium ore deposit in South China: geochronology, petrogenesis and relationship with uranium mineralization. *Lithos* 308-309, 118–133. doi:10.1016/j.lithos.2018.02.028

Zhang, C., Cai, Y. Q., Dong, Q., Xu, H., and He, S. (2019). Genesis of the South Zhuguang uranium ore field, South China: fluid inclusion and H-C-O-S-Sr isotopic constraints. *Appl. Geochem.* 100, 104–120. doi:10.1016/j.apgeochem.2018.11.008

Zhang, L., Chen, Z., Wang, F., White, N. C., and Zhou, T. (2021a). Release of uranium from uraninite in granites through alteration: implications for the source of granite-related uranium ores. *Econ. Geol. Bull. Soc. Econ. Geol.* 116 (5), 1115–1139. doi:10.5382/econgeo.4822

Zhang, L., Chen, Z. Y., and Wang, F. Y. (2021b). General characteristics and research progress in metallogenies of granite-related uranium deposits in South China. *Acta Petrol. Sin.* 37 (9), 2657–2676. doi:10.18654/1000-0569/2021.09.04

Zhang, L., Wang, F. Y., Zhou, T. F., and Chen, Z. Y. (2022). Contrasting U-Pb geochronology and geochemistry of uraninite from the Xianshi and Xiwang uranium deposits, South China: implications for ore genesis. *Ore Geol. Rev.* 149, 105120–15. doi:10.1016/j.oregeorev.2022.105120

Zhou, X. M. (2007). *The genesis and petrogenesis of late Mesozoic granites in the Nanling area and the dynamics of the lithosphere evolution*. Beijing: Science Press.

Zhu, J. C., Chen, J., Wang, R. C., Lu, J. J., and Xie, L. (2008). Early Yanshanian NE trending Sn/W-bearing A-type granites in the western-middle part of the Nanling Mts region. *Geol. J. China Univ.* 14 (4), 474–484. doi:10.3969/j.issn.1006-7493.2008.04.002

Zou, X. Y., Qin, K. Z., Han, X. L., Li, G. M., Evans, N. J., Li, Z. Z., et al. (2019). Insight into zircon REE oxy-barometers: a lattice strain model perspective. *Earth Planet Sci. Lett.* 506, 87–96. doi:10.1016/j.epsl.2018.10.031